Non-Invasive Positron Detector to Monitor the Arterial Input Function in Dynamic PET

LIAM CARROLL

MEDICAL PHYSICS UNIT

MCGILL UNIVERSITY, MONTREAL

AUGUST, 2019

A thesis submitted to McGill University

in partial fulfillment of the requirements

for the degree of Master of Science

ABSTRACT

Imaging and treatment of cancer has seen significant progress and innovations in recent years contributing to earlier diagnosis and more advanced, accurate and precise treatments than previously available. New targeted therapies and treatments are highly effective at killing specific tumor types but unfortunately not for all patients. Tests are needed to determine if a given cancer therapy is working. One highly effective, but underused method for such a test is by using dynamic positron emission tomography (dPET). This is a nuclear medicine imaging technique where positron emitting radioisotopes labelled with a molecule of interest is injected into the patient and tracked through their body. To perform dPET, the radiation activity concentration in the patient's blood, called the arterial input function (AIF), must be measured throughout the scan. dPET is underused in the clinic because there is no easy way to measure the AIF clinically. The current gold standard to measure the AIF is through arterial blood sampling which requires expensive, additional equipment and personnel such as anesthesiologists. It also causes great discomfort to the patient. To get around this barrier to entry, we have designed a non-invasive detector (NID) that is capable of measuring positrons emitting from the patient's wrist to determine the AIF during a dPET scan. Based on plastic scintillating fibers and by using a dual-readout system, the NID detects and localizes positrons in space. The NID was validated against a microfluidic detector designed for use with small animal dPET studies. A closed-loop microfluidic system was used to mimic a patient's circulatory system and a phantom was used to simulate attenuation by the patient's wrist. During the first experiment, three PET radioisotopes were tested ^{18}F, ^{11}C and ^{68}Ga. After improvements were made to the detector, a second series of tests were performed using only ^{18}F and ^{11}C. All tests were performed at clinically relevant activity concentrations. The maximum SNR that was obtained was 52.18 with the ^{11}C tests. Linear regressions showed that results obtained from both detectors matched very well ($slope = 0.93$, $R^2 = 0.99$ for the second ^{11}C test). These preliminary results show that the NID can accurately detect positrons escaping

a patient's wrist and has the potential to measure the AIF during a dPET scan.

RÉSUMÉ

Les traitements de cancers deviennent de plus en plus précis et puissants, mais aussi plus en plus spécifiques. A cause de cette spécificité, les nouveaux traitements ne fonctionnent pas pour chaque patient ce qui nécessite des tests d'efficacité pour chaque traitement. Les standards courant pour ces tests sont lents et ne sont pas toujours précis. Une autre option et d'utiliser la tomographie par émission de positrons dynamique (TEPd). Ceci est une modalité d'imagerie de médicine nucléaire ou le patient est injecté avec un traceur radioactif qui émit des positrons. Pendant un scan TEPd, le traceur est suivi pour faire une image des fonctions biologique du patient. Pour produire l'image finale, il faut savoir la concentration radioactive dans les artères, appelé la fonction d'entrée artérielle (FEA), du patient tout au cours du scan. Le TEPd est sous-utilisé dans les cliniques parce qu'il n'y aucune façon facile d'obtenir le FEA. Le standard pour obtenir le FEA consiste prendre du sang des artères des patients tout au long du scan, ce qui nécessite du personnel chirurgical supplémentaire et cause de grand inconfort pour le patient. Pour surmonter ce défi, nous avons développé un détecteur non-invasif (DNI) qui peut détecteur les positrons qui sortent des artères du patient pour déterminer le FEA. Ce détecteur utilise des fibres scintillantes en plastique pour détecter les positrons tout au long d'un scan TEPd. Le DNI a été validé contre un détecteur de type microfluidique qui a été conçu pour des études d'animaux. Pour la première teste, trois isotope TEP ont été testé : ^{18}F, ^{11}C and ^{68}Ga. Après que d'avoir amélioré le DNI, une deuxième teste a été performé avec ^{18}F et ^{11}C seulement. Un système microfluidique a été conçu pour imiter le système circulatoire du corps humain et nous avons utilisé un modèle pour simuler l'atténuation des positrons par le poignet du patient. On a obtenu un rapport signal sur bruit maximale de 52.18 avec le deuxième teste de ^{11}C. Une régression linéaire montre que les résultats obtenus par les deux détecteurs sont très proches ($pente = 0.93$, $R^2 = 0.99$ pour la deuxième teste avec ^{11}C). Ces résultats préliminaires montrent que le DNI peut détecter des positrons qui sortent du poignet d'un patient et a du potentiel pour mesurer le FEA.

Acknowledgements

I would begin by thanking my supervisor and mentor, Dr Shirin Abbasinejad Enger, who always pushed for more and was always willing to sit down and and answer questions about the project. Equally important is Dr. Gustavo Kertzscher, who is the co-inventor of the detector. He always offered frank advice and criticism, and kept the research on the right path. I would like to thank Dr. Roger Lecomte who gave us access to their facilities at Sherbrooke University Hospital and Dr. Etienne Croteau who helped us run experiments there. They handled all the radiation as I lack the requisite training and gave us a lot of feedback to improve the detector design. Lastly, I would like to thank my wife, Sara Postans, who had to endure hours of practice for the many presentations I gave over the course of this degree.

I also acknowledge support by the Natural Sciences and Engineering Research Council (grant 241018) and Collaborative Health Research Projects (grant 523394-18).

Contribution of Authors

Every chapter of this thesis was written by Liam Carroll. The main part of the thesis comes from experimental procedures performed at the McGill University Health Center, and Sherbrooke University Hospital.

For the experiments described in chapter 4, Dr. Gustavo Kertzscher created the protocol to build a scintillating fiber-based detector and gave general guidelines on the different measurements. Dr. Roger Lecomte provided lab space, radionuclide and radio-chemists to manipulate the radioactive solutions. Dr. Shirin Abbasinejad Enger supervised the work and provided general guidance.

Contents

List of Figures

List of Tables

List of Abbreviations

A.U.	Arbitrary Unit
AIF	Arterial Input Function
APD	Avalanche Photodiode
DPP	Digital Pulse Processing
FDG	FluDeoxyGlucose
FPGA	Field Programmable Gate Array
MRI	Magnetic Resonance Imaging
NID	Non-Invasive Detector
PET	Positron Emission Tomography
PMMA	Poly(Methyl MethAcrylate)
PLA	Polylactic Acid
PMT	PhotoMultiplier Tube
PS	Polystyrene
SiPM	Silicon PhotoMultiplier
SNR	Signal-to-Noise Ratio
UV	Ultraviolet

Physical Constants

Speed of light in vacuum $\quad c = 2.998 \times 10^8 \,\mathrm{m\,s^{-1}}$

List of Symbols

a	atomic radius	Å
A	activity	Bq
b	impact parameter	Å
C_a	radioactivity concentration in arterial compartment	$\mathrm{Bq\,mL^{-1}}$
C_f	radioactivity concentration in intersitial space	$\mathrm{Bq\,mL^{-1}}$
C_m	metabolized radioactivity concentration	$\mathrm{Bq\,mL^{-1}}$
C_{PET}	radioactivity concentration in PET pixel	$\mathrm{Bq\,mL^{-1}}$
E	energy	eV
E_{max}	maximum positron energy	eV
E_{mean}	average positron energy	eV
$I(x)$	photon beam intensity as a function of distance travelled	$\mathrm{lm/cm}$
$I(0)$	photon beam intensity before travelling any distance	lm
k_{ij}	rate transfer constant between compartment i and j	min
L	scintillator luminescence	lm
n	index of refraction	
R_{max}	maximum positron range	mm
R_{mean}	average positron range	mm
S	linear stopping power	$\mathrm{MeV/cm}$
S_{rad}	radiative stopping power	$\mathrm{MeV/cm}$
S_{col}	collisional stopping power	$\mathrm{MeV/cm}$
S_{col}^{m}	mass collisional stopping power	$\mathrm{MeVcm^2/g}$
S_{col}^{soft}	soft collisional stopping power	$\mathrm{MeV/cm}$
S_{col}^{hard}	hard collisional stopping power	$\mathrm{MeC/cm}$
S_0	normalization constant of the PMT signal	A.U.
$S(x)$	PMT signal at position x	A.U.
S_i	singlet state of electron	
T_i	triplet state of electron	
$t_{1/2}$	half-life	s
v	velocity	$\mathrm{m/s}$
w	weight	kg
Z	atomic number	
τ	scintillator time constant	s
τ_1	time constant describing the population of the excited states in scintillator	s
λ	decay constant	$\mathrm{s^{-1}}$
λ_a	1/e attenuation length	cm
μ	linear attenuation coefficient	$\mathrm{cm^{-1}}$
μ_m	mass linear attenuation coefficient	$\mathrm{cm^2/g}$

This thesis is dedicated to my cats, Cléopatre and Nefertiti. Without them, this work would have been completed one month sooner.

Chapter 1

Ionizing Radiation Interactions in Scintillators

Ionizing radiation cannot be seen, heard or felt. It leaves no taste on the tongue and no scent in the air. In fact, the human body is without recourse when it comes to sensing ionizing radiation, which is why we rely on specialized tools to do the sensing for us. These tools are called radiation detectors and come in a wide variety of shapes with many different mechanisms of action.

Scintillator-based detectors are but one of many ways to detect, and quantify ionizing radiation. This work focuses on a novel scintillating detector for use with dynamic positron emission tomography (dPET). Chapter 1 explains the physics of scintillators, chapters 2-3 go into detail concerning the different components of a scintillator detector system and the remaining chapters explore the detector we built and its applications.

Ionizing radiation is defined as radiation with sufficient energy so that it can excite and ionize atoms of matter. This energy is on the order of 4-25 eV (Williamson, 2018), and can be carried by one many different types of particles. These particles can be divided into four categories with respect to how they interact with matter.

1. Heavy charged particles: protons, heavy ions, mesons
2. Light charged particles: electrons and positrons

3. Electromagnetic radiation: photons
4. Neutrons

The first two categories consists of charged particles and the second two consist of uncharged particles. It is extremely important to note that only charged particles deposit energy to a medium. Uncharged particles deposit energy in a indirect fashion as they will first produce charged particles in the medium which in turn will deposit their energy. Thus, charged particle radiation can be called directly ionizing and uncharged particles can be called indirectly-ionizing (Williamson, 2018). The rest of this section will focus on the interactions of electrons/positrons and photons, as these are the important particles with regards to this work.

1.1 Photons

The manner in which a photon interacts with matter varies based on its energy and the material that it is interacting with. Figure 1.1 shows the three most important photon interactions and their relative probabilities. Notice that the probabilities are dependent on the photon energy and the atomic number Z of the interacting matter. Compton scattering also depends on the electron density of the iteracting matter. The result of photoelectric absorption or pair production is the complete absorption of the original photon and the excitation or creation of free charged particles. The Compton effect produces a free electron, however, the incoming photon is scattered, traversing the medium now with a lower energy and can interact again.(Podgoršak, 2006; Williamson, 2018). There also exists *Rayleigh scattering*, which results from a photon interacting with an orbital electron and simply changing direction. This interaction does not impart any energy to the medium but could scatter the photon out of the beam.

When a photon interacts in one of the above manners, it may transfer some or all of its energy to charged particles, which then deposit their energy in the medium or scatter

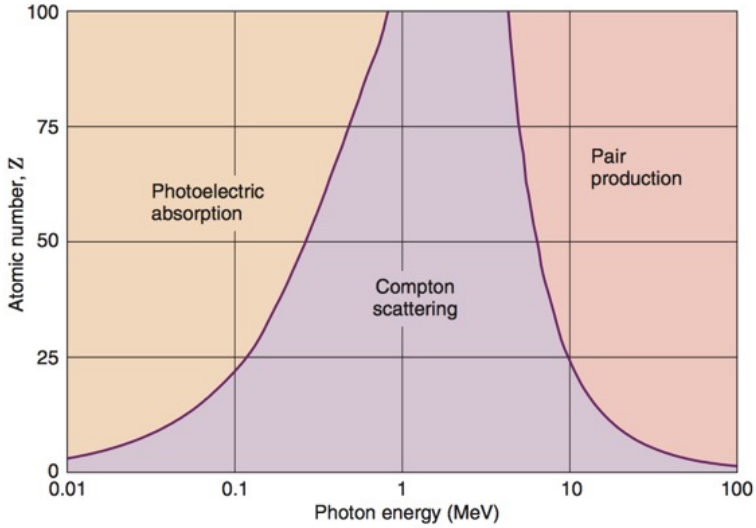

FIGURE 1.1: Plot showing the relative probabilities of the three most important photon interactions with matter. Often called the "Curtain Plot" Figure taken from (Cherry, Sorenson, and Phelps, 2012)

out of the beam. Each interaction type has its own probability of occurring. These processes are collectively called beam attenuation. This can be described as follows.

$$I(x) = I(0)e^{-\mu x} \tag{1.1}$$

where $I(x)$ is the beam intensity after it has travelled a distance x through the medium. In this case, μ is called the *linear attenuation coefficient* of the medium and is measured in inverse unit lengths (m^{-1}). The probability of photon interaction per unit distance traveled in the medium is obtained by μ. Note that μ changes based on the energy of the photon beam and the composition of the medium. By setting $I(0) = 1$, the above relationship can be used to determine the probability of a single photon not interacting as it travels through a medium.

The total linear attenuation coefficient for a given photon beam in a give medium is a sum of the linear attenuation coefficient of all four interactions mentioned above. A more commonly used value is the mass attenuation coefficient (μ_m), which is simply $\mu_m = \mu/\rho$, where ρ is the density of the material. Figure 1.2 shows the μ_m for carbon and lead. Note how the values are much greater in the lead graph, this is due to Z

dependence of μ_m (Podgoršak, 2006; Williamson, 2018).

1.2 Light Charged Particles

Charged particles interact much more frequently with atoms than uncharged particles due to the Coulomb interactions with the charged electrons and nuclei of the medium. For electrons and other light charged particles, this causes frequent changes in direction of travel and results in a very torturous path such that the total path length is much larger than the absolute distance travelled. There are three types of interactions that can occur from charge particle interaction with matter as shown in figure 1.3. The type of collision that occurs is based on the impact parameter b, which is the perpendicular distance between the initial velocity vector of the charged particle and the center of the atomic nucleus and the atomic radius a of the medium.

Hard Collision: $b \approx a$

When b is on the order of a, the charged particle will have a direct collision with a single orbital electron, called a *hard collision*. This will eject the orbital electron with enough energy so that it may also undergo Coulomb interactions. Although hard collisions are relatively rare, they cause a large loss of energy for the incident particle.

Soft Collision: $b >> a$

When b is much larger than a, the charged particle interacts with the atom as a whole, changes direction and impart a small fraction of its energy to the atom. This can excite the atom by raising an atomic electron to a higher orbital, or by ejecting a valence electron. These interactions impart much less energy than hard collisions, but occur much more frequently.

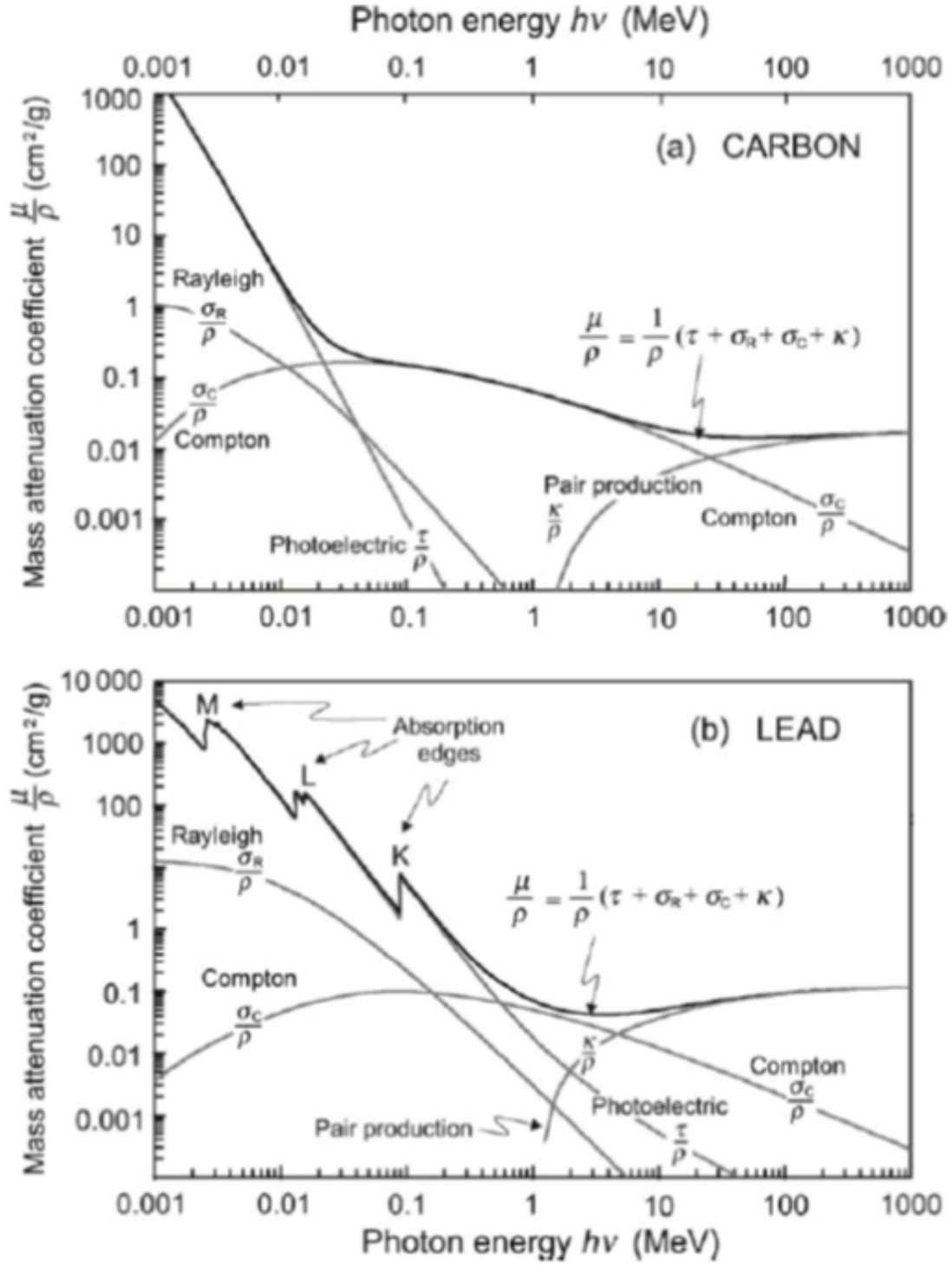

FIGURE 1.2: Mass attenuation coefficients for (a) carbon and (b) lead and various photon energies. Figure taken from (Podgoršak, 2006)

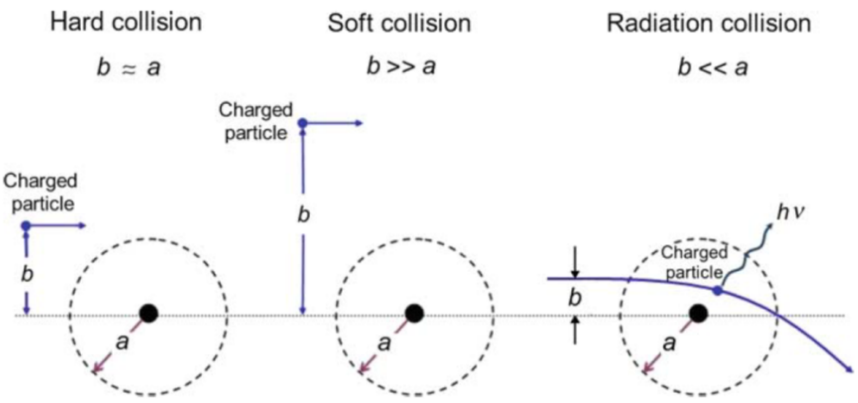

FIGURE 1.3: Three possible interactions types for charged particles with an atom. These depend on the atomic radius a and the impact parameter b. Figure taken from (Podgoršak, 2006)

Radiative Collision: $b << a$

When b is much smaller than a, the charged particle will interact primarily with the charged nucleus. This will cause the incident particle to change direction or momentum. Most of the time, there is an insignificant energy loss by the particle. Sometimes, the collision is inelastic and the incident particle losses a significant amount of energy. This is accompanied by the emission of an x-ray photon called a *brehmstrahlung emission*. Note that such an emission must occur in the electric field of an atomic nucleus.

1.2.1 Stopping Power

The total energy loss by a charged particle in a given medium is a combination of the energy loss through all three collision types and the rate of energy loss is described by the *linear stopping power (S)*. This is the mean energy loss per path length in a given medium by a charged particle of a given energy. It is composed of S_{col}, the energy loss due to hard and soft collisions, and S_{rad}, the energy loss due to radiativ collisions. S_{col} can be divided into $S_{col}^{soft} and S_{col}^{hard}$, the energies lost to soft and hard collisions respectively.

$$S = S_{rad} + S_{col} = S_{rad} + S_{col}^{soft} + S_{col}^{hard} \tag{1.2}$$

As seen above, charged particles can directly deposit energy to the medium, eject secondary electrons and cause emission of photons. Even if a charged particle looses all of its energy in a given a medium, it is possible for some of this energy to escape due to radiative collisions. Because of this, when trying to determine how much energy is deposited in a medium, S_{col} is used. The reason for this is that S_{col} excludes any energy lost to photons that have a high chance of escaping. Furthermore, this only holds for charged particles with lower energy. Higher energy particles would have a higher likelihood of escaping the medium and depositing their energy elsewhere. Similar to photon attenuation coefficients, the more commonly used value is the mass collision stopping power S_{col}^{m}. Figure 1.4 shows S_{col}^{m} for electrons in water, Al and Pb. Note that S_{col}^{m} is dependent on the number of electrons per unit mass and slowly decreases with higher Z. The radiative stopping power increases with Z and with electron energy. This shows that the higher the electron energy, the more energy will be lost to bremsstrahlung emissions.

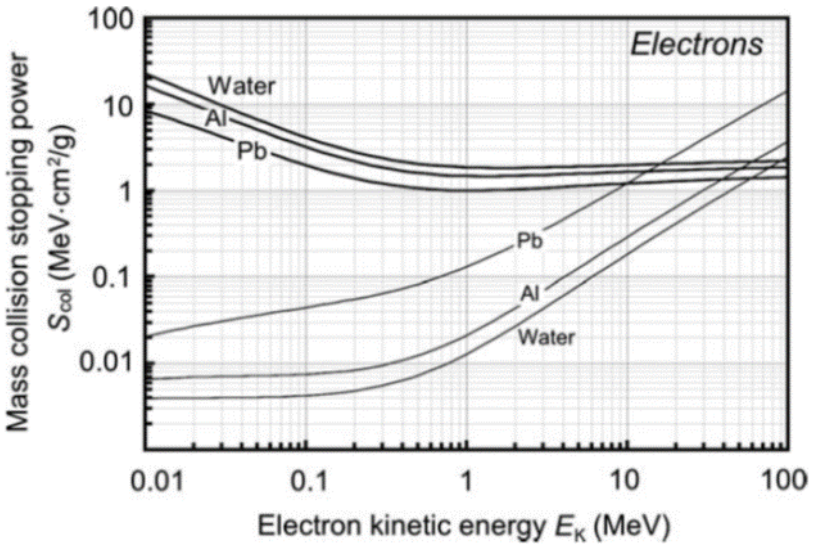

FIGURE 1.4: Mass collision stopping power for electrons travelling through water aluminum and lead. Collision stopping powers shown in thick lines, radiative stopping powers shown in thin lines. Figure taken from (Podgoršak, 2006)

Chapter 2

The Physics of Organic Scintillators

Scintillating materials, or scintillators are a class of material that interact with ionizing radiation to produce low energy photons. There are two main categories of scintillators, organic and inorganic. The organic scintillators are divided into three categories, plastic, liquid, and crystal. Of the three, plastic organic scintillators are the most widely used and will be the focus of this work. Hereon, any mention of scintillators refers to plastic organic scintillators.

2.1 Plastic Scintillator Basics

Organic plastic scintillators are materials that generally have low Z, and densities near that of water (1.03 to 1.20 $\mathrm{g/cm^3}$). They produce optical photons in the blue/green wavelengths and have two principle components, the plastic base and fluors whose specific roles will be described later (Nakamura, 2010). There are different processes that can cause the emission of visible radiation from a substance. *Fluorescence* is defined as "the prompt emission of visible radiation from a substance following its excitation by some means." (Knoll, 2010) *Phosphorescence* is distinguished from *fluorescence* by the longer wavelength of the emitted radiation and a slower characteristic time. *Delayed fluorescence* results in the same wavelength of emitted light as prompt fluorescence, but with a much longer emission time (Knoll, 2010).

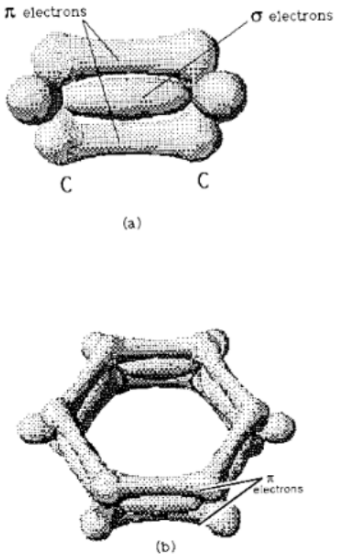

FIGURE 2.1: (a) shows a side-view of π electron bonds and a σ electron bond. These are regions of high electron density. (b) Shows the π electrons in a benzene-ring, a common aromatic structure. Figure taken from (White, 1988)

2.2 Scintillation Mechanism

Efficient organic scintillators are composed of molecules that have π electrons commonly found in aromatic, or ring shaped, molecules. Figure 2.1 shows an example of a structure with π electrons. π electrons are desirable because they are free to move around their respective rings and due to their possible energy levels (White, 1988). Figure 2.2 shows the energy levels of a plastic scintillator. Notice that there are singlet states and triplet states. The singlet state corresponds to electrons with a spin quantum number of 0 while the triplet state corresponds to a spin quantum number of 1. The principle singlet states (S_i) are divided into vibrational states (S_{ij}) which are normally spaced about 0.15 eV apart. With this nomenclature, S_{00} represents the ground state. Thermal energies are normally around 0.025 eV, so are unlikely to provide enough energy to promote the electrons to an exited state. The molecules are thus normally in the grounds state. To go along with the singlet states, there are a number of possible triplet states represented by T_i. These states are comparatively lower in energy than the corresponding singlet states so it would be possible for a singlet state electron to

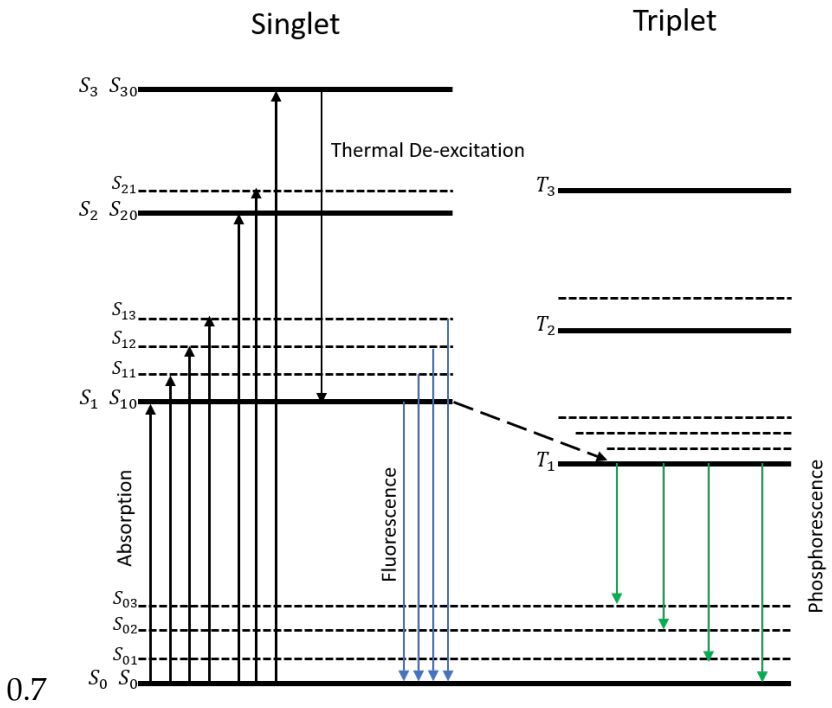

0.7

FIGURE 2.2: π electron energy levels in an organic molecule. Black arrows represent non-radiative energy transitions, colored arrows represent radiative energy transitions

become a triplet state electron with no extra energy needed.

The process of scintillation starts when an ionizing particle crosses a scintillating material and deposits energy through one of the mechanisms described above. This results in a molecule with excited electronic (rotational and vibrational) levels, which takes about $0.5\,\mathrm{ns}$ (Leutz, 1995; Knoll, 2010) depending on the scintillating material. Any electron in a higher electronic or vibrational state, for example S_{12} would not be in thermal equilibrium with its neighbors and would de-excite down to the S_{10} state. This occurs on the ps time-scale and results in a population of electrons in the S_{10} state very quickly after the passage of a charged particle. The prompt fluorescence emission is due to the transition between the S_{10} state and one of the vibrational levels of the primary singlet state (S_0), which normally occurs after a couple of ns and depends on the scintillator. The intensity of the fluorescent light follows an exponential decay and can be represented by

$$I = I_0 e^{-t/\tau} \tag{2.1}$$

where τ is called the decay time of a scintillator. This equation does not take into account the finite time it takes the electrons to initially populate the excited energy states. Taking into account the finite rise time, equation 2.1 can be expanded

$$I = I_0(e^{-t/\tau} - e^{-t/\tau_1}) \tag{2.2}$$

where τ_1 is the time constant describing the population of the excited states. We now have a description of how the prompt fluorescence occurs.

As noted above, the triplet states are all at a lower energy level than their corresponding singlet states. This allows the electrons to cross from singlet to triplet in a process called *intersystem crossing*. These triplet state electrons can then relax down to the base S_0 state through phosphorescence,which is much slower process and can take up to several milliseconds to complete. Furthermore, the phosphorescent light is of a longer wavelength than the fluorescent light so will yield a delayed spectrum that differs from the fluorescence spectrum. Some of the triplet electrons can be thermally excited back to the a singlet state and decay by fluorescence. This is the cause of the delayed fluorescence in organic scintillators.

Note in figure 2.2 that all of the upwards arrows are longer than the downwards arrows, except for the S_{00} to S_{10} arrow showing that light emitted from a scintillator will not re-excite it. Most organic scintillators are transparent to their own emissions. If a plot was made of the emission and absorption wavelengths of a given scintillator, there would be two separate peaks and some overlap near the middle. The distance between the two peaks is called the *Stokes shift*. An example of this is shown in figure 2.3.

There exists other de-excitation modes for the excited electrons which causes some loss

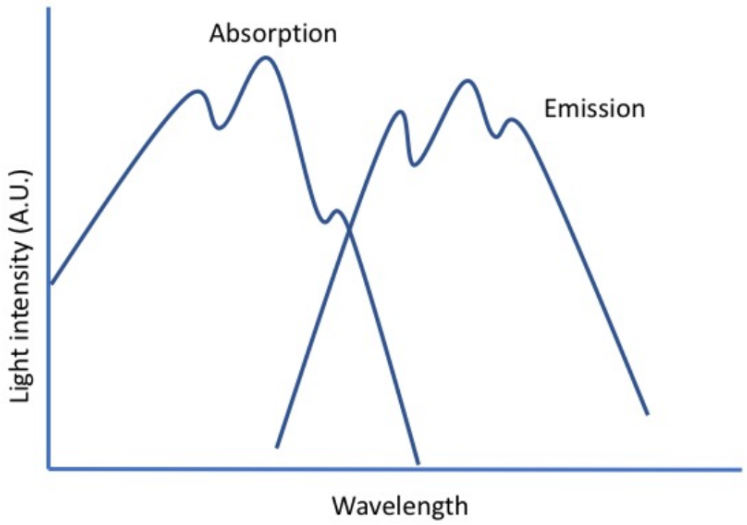

FIGURE 2.3: Example of an organic scintillator's Stokes shift. Figure taken from (Knoll, 2010)

of fluorescence. The sum of all these other mechanisms are called *quenching* and reduce the *scintillating efficiency* of an organic scintillator. Furthermore, not all fluorescence photons will escape the scintillator as some will be attenuated along the way. The distance that scintillated light will travel in the scintillator before being attenuated to $1/e$ of its original number of photons is called the *attenuation length* of a scintillator.

2.3 Scintillator Components

The most common base plastics in organic scintillators are polystyrene (PS) and polyvinyl toluene. While these materials will readily become excited by ionizing radiation, some of their other properties are not ideal. Their fluorescent emissions are in the UV range, which are hard to detect by modern photodetectors and has an attenuation length of several mm. Without extra help, very few of the fluorescent photons would escape the scintillator. They also have relatively long τ, on the order of 10s of ns. This is not ideal, because this would represent the maximum timing resolution that is possible with these plastics. To overcome these deficiencies, the base plastics are usually mixed with two or more organic scintillators called fluors.

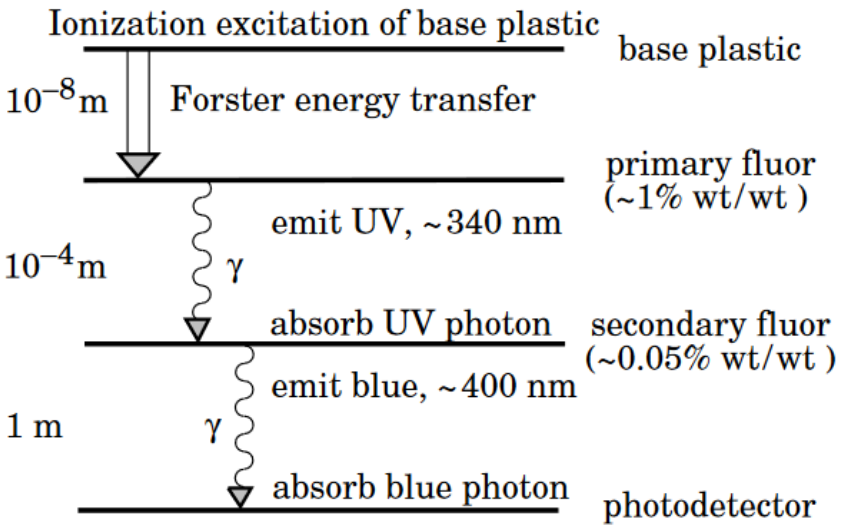

FIGURE 2.4: Energy transition schematic of a plastic scintillator using two fluors. (Nakamura, 2010)

The first fluor in a given scintillator is chosen such that the emission spectrum of the base plastic matches the absorption spectrum of the fluor and is included at about 1% by weight. This has multiple effects. Firstly, the photons emitted by the base will be absorbed and re-emitted at longer wavelengths by the fluor, which accounts for around 20% of the photons emitted by a scintillator (Swank and Buck, 1953). The other 80% is due to non-radiative energy transfers between the base plastic and primary fluor. At the concentrations added, a molecule of fluor will be no more that 100 Å from an excited base unit. The energy transfer occurs via resonant dipole-dipole interactions called *Forster energy transfer*, which increases the speed and yield of these scintillator.

Almost always, the primary fluor will also have undesirable emission spectra and attenuation length, so a secondary or even a tertiary fluor is needed. Figure 2.4 shows a schematic of the energy transition diagram for a plastic scintillator with two fluors. Notice that the primary fluor often emits UV photons with very short attenuation lengths. (Nakamura, 2010; Birks and Firk, 1965; Knoll, 2010; Leutz, 1995)

2.4 Light Output

The amount of light that is produced by a scintillator is dependent on the energy deposited in it. Ideally, this would be a linear dependence, but is not always the case. When a scintillator is irradiated with electrons or protons, its luminescence L has the following relationship to the energy deposited E along a path of length x:

$$\frac{sL}{dx} = S * \frac{dE}{dx} \tag{2.3}$$

where S is the scintillation efficiency. This is a linear relationship and holds for electrons above 125 keV. If the ionization density in the scintillator increases, then equation 2.3 will eventually no longer hold. An increase in ionization density is caused by an increase in radiation intensity, i.e. more electrons per second, or a change in particle type to a heavier charged particle with denser ionization tracks, e.g. protons or alpha particles. In either case it results in lower luminescence than predicted from the linear relationship. Birks (Birks and Firk, 1965) suggests that this is caused by quenching due to damaged molecules along the high ionization density tracks. The density of damaged molecules along the ionization track can be represented by $B(dE/dx)$, where B is a proportionality constant. Some fraction k of these damaged molecules will lead to quenching and a reduction in the light yield. We can modify equation 2.3 to take this into account.

$$\frac{dL}{dx} = \frac{S * \frac{dE}{dx}}{1 + k_B \frac{dE}{dx}} \tag{2.4}$$

In the equation above k_B is called *Birk's constant* and represents the damaged molecules that lead to quenching. The proportionality constant k_B must be measured for each scintillator by irradiating a scintillator with a known amount of radiation and measuring the output while increasing the radiation intensity. The resulting data points can fit to equation 2.4. (Knoll, 2010; Birks and Firk, 1965)

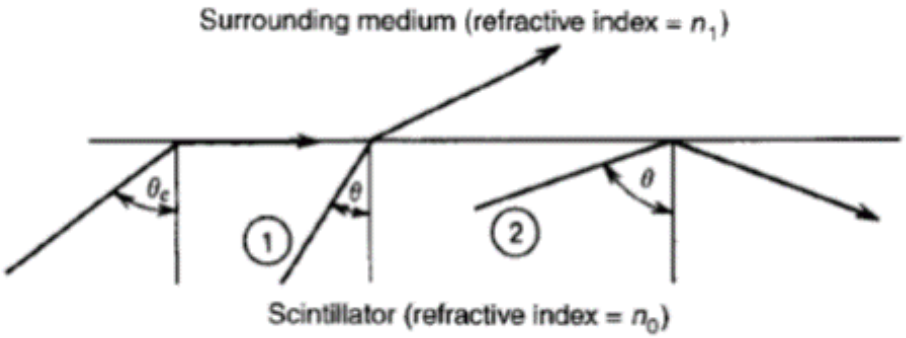

FIGURE 2.5: Schematic showing that photons with angles of incidence greater than a critical angle will be reflected at a media interface. Figure taken from (Knoll, 2010)

2.5 Plastic Scintillating Fibers

Scintillating fibers consist of long strands of scintillators with a protective coating on the outside called cladding. This cladding is needed to prevent the sensitive scintillator from being damaged. The fibers allow for the collection and transportation of light over relatively long distances via total internal reflection. When light crosses a boundary between two media, it will reflect back into the media of origin, called *total internal reflection*, or it will undergo partial reflection, called *Fresnel reflection*, and partial transmission through the boundary. The closer the angle of incidence is to 0, the more light will pass through. The critical angle θ_c is defined by the indices of refraction of the origin medium n_0 and the surrounding medium n_1.

$$\theta_c = sin^{-1}(\frac{n_1}{n_0}) \tag{2.5}$$

This is represented graphically in figure 2.5. Notice how the photon's angle of incidence controls the reflection angle of the photon. As the angle of inidence increases, so does the angle of reflection.

Since scintillation light is emitted isotropically, much of it will escape. The usual solution to this is to wrap the scintillator in a reflective material, but this is often not

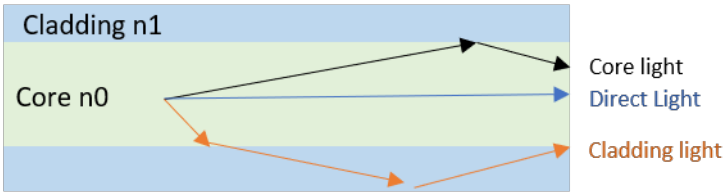

FIGURE 2.6: Schematic of a single clad plastic scintillating fiber

possible for scintillating fibers. As a result, the light capture fraction is quite small and can be described by the following equation:

$$F = \frac{1}{2}(1 - \frac{n_1}{n_0}) \tag{2.6}$$

where n_0 and n_1 represent the indices of refraction of the scintillator core and the cladding respectively and F represents the fraction of photons that will propagate down one end of the fiber called the *capture fraction*. Since a fiber has two ends, the total captured light is double equation 2.6. As an example, a fiber with a standard PS scintillator core and a polystyrene cladding would have indices of refraction $n_0 = 1.58, n_1 = 1.49$. Equation 2.6 would yield a capture fraction of 2.8% per fiber end.

To complicate things further, some photons that escape the core may get captured in between the cladding and the outside media. Figure 2.6 shows an example of these photons which are called *cladding light* and represent a small fraction of the collected light. Furthermore, the captured photons will travel at different speeds as some will be reflected many times as they pass through the fiber and a small fraction will travel straight down. These are called *core light* and *direct light* respectively.

The cladding protects the plastic core, but also reduces the capture fraction due to having an index of refraction closer to that of the core. To improve the collection efficiency, a second cladding material is sometimes added outside the first with a lower index of refraction. These fibers are called multiclad fibers and have an improved collection efficiency of around 40%.

Once the light is trapped in the fiber, it travels down its length and eventually reaches

the end where it will be collected by a light sensitive device. The intensity of the light will gradually decrease as photons are attenuated due to different effects, such as:

- Imperfections at the core/cladding interface which will reduce the amount of total internal reflection.
- Re-absorption of the scintillating photons due to overlap of the emission/absorption bands.
- Photons that scatter out of the core due to small density changes.

Added together, these processes can be described by the *attenuation length* (λ_a) of a fiber. λ_a is the distance a photon packet can travel before being reduced to $1/e$ of its starting intensity. At first approximation, this attenuation of the captured light intensity can be approximated by an exponential decay function.

$$I(x) = I_0 * e^{-x/\lambda_a} \tag{2.7}$$

where $I(x)$ is the light intensity as a function of path length travelled and I_0 is the initial light intensity. This equation is generally assumed to hold but in reality, the photons with shorter wavelengths become attenuated sooner than the others. After a certain distance, most of the short wavelength photons will be attenuated. We are left with a situation where the attenuation will be greater at short distances, and less at long distance. (Birks and Firk, 1965; Knoll, 2010; White, 1988; Leutz, 1995)

2.6 Scintillating Fiber Read-Out

As described in the above sections, scintillating fibers produce visible light in the presence of ionizing radiation. This light travels down to both ends of the fiber. To get a measurable electric signal, the photon energy needs to be converted to an electric

charge or current, a task that is accomplished by using photodetectors. There are two types of photodetectors that are of interest for our detector design:

- photomultiplier tubes (PMTs)
- Silicon Photomultipliers (SiPMs)

2.6.1 PMTs

PMTs are analog electronic devices that produce a measurable current from single photons, or packets of photons. These devices work by converting photons in the visible light range into free electrons in a process called *photoemission*. These electrons are then accelerated and multiplied to produce a large enough signal to be measurable with common electronics. PMTs can produce up to $10^6 - 10^7$ electrons per absorbed photon. Figure 2.7 shows a general diagram labeling the different PMT components.

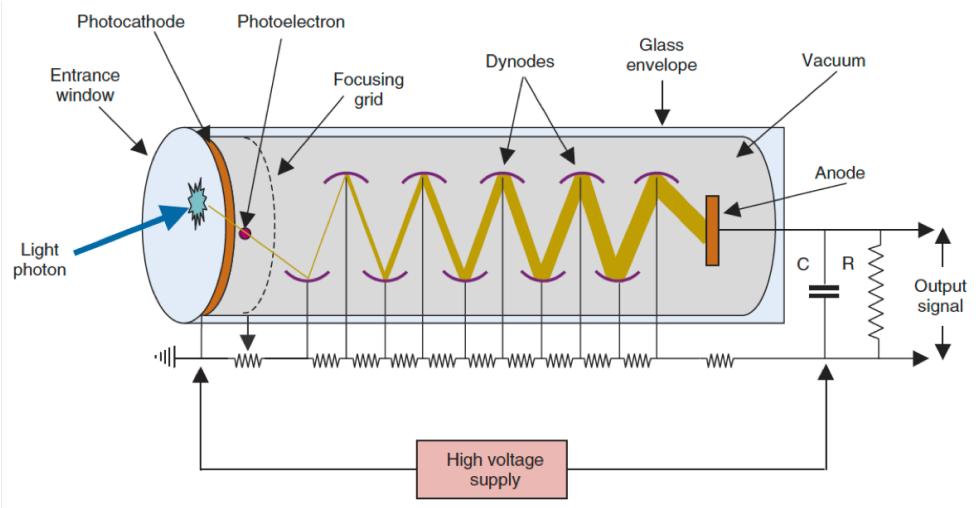

FIGURE 2.7: Schematic showing how PMTs function. Figure taken from (Cherry, Sorenson, and Phelps, 2012)

The photoemission process begins with a photon striking the PMT window and exiting an electron. This excited electron will migrate to the inner surface of the window where it can escape into the PMT. The inner volume of the PMT is kept under vacuum and is kept in an electric field. The negatively charged inner window surface, also called the *photocathode*, and positively charged anode at the other end of the PMT, produce

this electric field. The effect of the field is to help electrons escape the window and to accelerate them through the PMT towards a series of electrodes called *dynodes*.

When the electrons strike a dynode, they deposit their kinetic energy and cause the dynode to emit multiple electrons for each incident electron. Typical PMTs with 10 dynodes in succession will create a cascade effect where one photoelectron can produce $10^6 - 10^7$ electrons by the time the final dynode is passed. The final set of electrons are collected at the anode to produce an electric charge that is proportional to the total energy of the photons incident on the PMT. (Cherry, Sorenson, and Phelps, 2012; Knoll, 2010).

2.6.2 SiPMs

A second common photodetector is the silicon photomultiplier. These detectors are composed of arrays of conventional *photodiodes* operating in the Geiger regime. To understand this, let us first examine the features of a single photodiode.

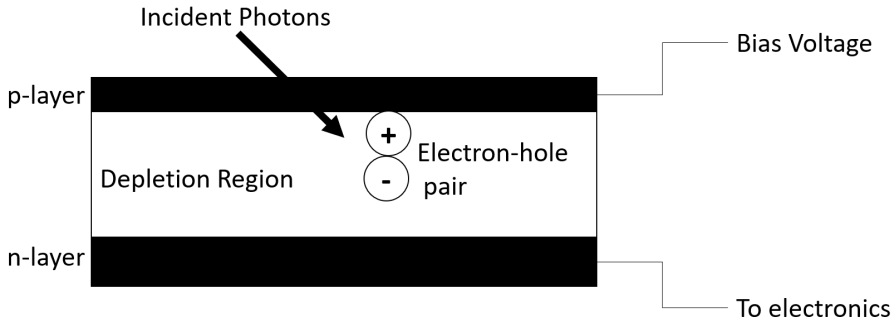

FIGURE 2.8: Schematic of a basic photodiode

Figure 2.8 shows the basic components of a photodiode. These devices are constructed out of a semiconducting material, often silicon, with p and n-layers on opposite sides. The p-layers are electron depleted, and are thus positively charged while the n-layers are negatively charged, with excess electrons. When a photon passes through the diode, it will form an electron-hole pair and a bias voltage placed across the wafer drives the charge carriers to create a small current. With a small bias voltage, one

electron-hole pair per photon is created. This would create a very small and very difficult signal to measure. Luckily, there are ways to amplify this signal.

By increasing this bias voltage, an internal gain can be implemented with multiple charge carrier pairs being produced from a single photon. This results in a linear gain. If the bias voltage is sufficiently high, the gain will no longer be linear, but will still be proportional to the applied voltage This is called the linear regime of the dope. Increasing the bias voltage further will cause the diode to enter the Geiger-Müller regime. Any single photon passing through the diode will cause an avalanche effect where the diode will completely discharge, producing a large signal that is no longer proportional to the number of incoming photons. Photodiodes operating in the Geiger-Müller regime are called *Avalanche photodiodes (APDs)*.

An SiPM consists of many thousands of APDs operating on the same circuit. In this way, any single photons that interacts with one of the APD sub-units will cause the APD to discharge and add to the output signal. The output voltage of an SiPM will be the accumulation of all of the signals of all of the APDs which have fired-off in response to individual photons. In this way, the signal from an SiPM is quantized, with the smallest unit being a single APD firing due to a single photon entering the detector. This means that SiPM are not truly analog and have distinct voltage levels that can they can output. This quantized nature is also the source of error from SiPMs. At higher incident photon intensities, it becomes increasingly likely that two or more photons will strike the same APD subunit. If this occurs, the second and subsequent photons will not be registered by the SiPM and the final signal will be smaller than the true signal. This is a phenomenon that can be measured and accounted for if an experiment will be operating at such high photon intensities. For the use of SiPMs with scintillating fibers, this is not normally a concern due to the low yield that the fibers produce. While SiPMs have a lower gain than traditional PMTs, their low cost and high timing performance make them ideal for many detector designs (Knoll, 2010).

Chapter 3

The Non-Invasive Detector (NID)

When designing a novel radiation detector, it is important to have rigid requirements that the detector must meet. These requirements are normally derived from the function that the detector will fulfill. This chapter will first motivate the need for the developed non-invasive detector (NID) and later explain the steps taken toward its design.

3.1 Detector Motivation

3.1.1 Cancer Treatment Efficacy

Modern cancer treatments can take many forms, from radiation therapy to chemotherapy and, more recently, targeted therapies. With these more advanced treatment techniques, it is ever more important to evaluate whether a patient's tumor is responding and dying, or is continuing to grow and spread (Michaelis and Ratain, 2006). Current standards for evaluating therapy efficacy involve using medical imaging techniques, such as computed tomography (CT) or magnetic resonance imaging (MRI) to measure a change in tumor size. This is problematic because the efficacy of newer cancer therapies cannot always be properly evaluated by measuring a change in tumor size (Eisenhauer et al., 2009). Other methods to evaluate be treatment response do exist, such as the promising modality 18-fluorodeoxyglucose (FDG) dynamic positron emission

tomography (dPET) (Strauss et al., 2011; Strauss, Pan, and StraussMD, 2010; Strauss et al., 2007).

3.1.2 Positron Emission Tomography

Positron emission tomography (PET) is a nuclear medicine imaging technique with a wide range of uses including cancer detection and monitoring, diagnosis of heart disease and neuro-degenerative disorders, and to help characterize novel pharmaceuticals (Cherry, Sorenson, and Phelps, 2012; Driessen et al., 2017; Takesh, 2012; Grkovski et al., 2017; Geus-Oei et al., 2006). These scans track the location of molecules of interest through the patient's body so that the pharmacokinetics of these molecules can be monitored. This is made possible by chemically bonding positron emitting radioisotopes to the molecules of interest before injecting them into the patient. Table 3.1 shows a selection of the most commonly used isotopes in PET imaging along with some of the properties of the positrons they emit.

TABLE 3.1: Properties of commonly used PET radioisotopes. Values from (Champion and Le Loirec, 2007)

Isotopes	Half-life (min)	E_{mean} (keV)	E_{max} (keV)	R_{mean} (mm)	R_{max} (mm)
^{18}F	109.8	252	635	0.66	2.633
^{11}C	20.3	390	970	1.266	4.456
^{13}N	9.97	488	1190	1.730	5.752
^{15}O	2.07	730	1720	2.965	9.132
^{68}Ga	68.1	844	1899	3.559	10.273

The principle behind PET is that the emitted positron will travel a short distance, on the order of millimeters, and then undergo *annihilation* with an electron. This is an interaction where the mass of the electron and positron is completely converted into two photons. These photons are emitted with anti-parallel velocities and energies of 0.511 MeV. PET scanners detect pairs of annihilation photons and use complex logic to determine if any two photons originated from the same positron annihilation event. Further discussion on the details of PET imaging are beyond the scope of this work

and readers are referred to (Cherry, Sorenson, and Phelps, 2012) for a more complete description.

3.1.3 Dynamic Positron Emission Tomography

In contemporary nuclear medicine clinics, PET scans can be performed with two different acquisition modes: static, or dynamic. Static PET scans make up the bulk of PET scans performed clinically. These scans involve injecting a patient with a radioatracer and waiting a period of time to allow the tracer to be distributed throughout the patient's body. Short acquisitions (5-10 min) can then be taken of the patient (Cherry, Sorenson, and Phelps, 2012). This is in contrast to dPET scans, where the acquisition starts at teh moment of radioatracer injection. As will be seen below, more complex modelling is performed on these scans to yield additional quantitative information.

We can now discuss dPET and *pharmacokinetic models*. These models are mathematical representations of a region of interest in the human body and are used to model the PET data. In the context of cancer imaging with FDG, the most commonly used model is a three-compartment model where each compartment represents a state that the tracer can inhabit (Bentourkia and Zaidi, 2007). Figure 3.1 shows a graphic representation of this model where C_a represents the tracer in the arterial blood, C_f represents tracer in the interstitial space and C_m represents the metabolized tracer in the tissue. The C_{PET} value is what a PET scanner is able to acquire and is a combination of all three compartments. It would be very difficult to determine the ratio of signals that originated from each individual compartment without further input. In the model, the k-values represent the rates of change of the tracer moving from one compartment to another. These are called pharmakokinetic parameters and are the values of interest when performing kinetic modelling (Bentourkia and Zaidi, 2007; Gunn, Gunn, and Cunningham, 2001).

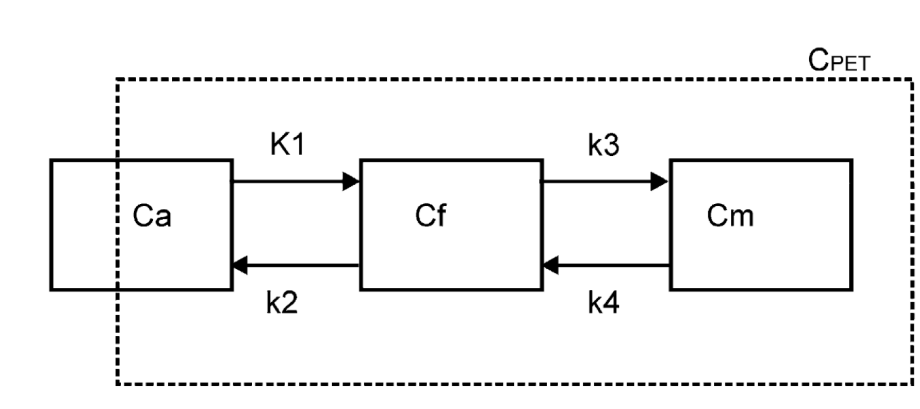

FIGURE 3.1: Three-compartment model often used in FDG dPET imaging. Figure taken from (Bentourkia and Zaidi, 2007)

The flow of radiotracers through these models can be explained using a series of differential equations. Solving these equations yields these k-values. Solving these equations yields an equation that is a function of the k-values and the C_a value. The C_a value represents the activity concentration in the patient's blood and is called the *arterial input function (AIF)* of a patient, which is required to solve for the k-values and perform kinetic modelling (Bentourkia and Zaidi, 2007; Gunn, Gunn, and Cunningham, 2001).

3.1.4 Acquisition of the AIF

Traditionally, the AIF was acquired through sampling of the patient's arterial blood throughout the scan (Phelps, Mazziotta, and Schelbert, 1986). This invasive procedure causes discomfort to the patient, is expensive and exposes the medical personnel to potential radioactive contamination while collecting the samples. Furthermore, the achievable temporal resolution using manual sampling can prevent the accurate determination of the AIF peak.

Due to these limitations, there are several other methods that have been developed to determine the AIF. These include automatic blood samplers, image-derived input functions and population based input functions (Litton and Eriksson, 1990; Watabe et al., 2001; Watabe et al., 2006; Knowland et al., 2018; Geus-Oei et al., 2006). Unfortunately, all of these methods introduce various errors and require different corrections.

3.1.5 Automatic Blood Samplers

Automatic samplers still require invasive implantation of the blood collector in patient's artery (Boellaard et al., 2001). The AIF measured by these samplers differs from the AIF at the tissue of interest due to two principle effects: dispersion and delay. The time it takes the blood to travel from the patient's artery to the blood sampler will differ from the time it takes the blood to travel to the tissue of interest. This is called the delay effect and needs to be measured and corrected for, otherwise the measured AIF will be shifted in time when compared to the true AIF.

The initial radiotracer injection into the patient is performed over a short perior of time. This results in a large concentration of radiotracer immediately after injection called a *bolus.* As the bolus travels through the patient's circulatory system, it will become more dispersed. The further the bolus travels, the more dispersed it will become. Since the blood is not sampled from the tissue of interest, there will be a dispersion difference between the blood at the sampler and the blood at the tissue of interest. This needs to be corrected for and is called the dispersion correction. (Lüdemann et al., 2006)

3.1.6 Image-Derived Input Functions

Image-derived input functions are methods that use the PET signal from part of the image to determine the input function. Ideally, these methods would use a large blood-volume in the scanner field-of view, such as the left ventricle or the aorta. For many dPET scans, this condition is difficult to meet as there are no large blood volumes near the region of interest. One notable exception to this are dPET scans imaging the heart. If a smaller blood volume is used, the partial volume effect will add errors to the AIF. The partial volume effect is due to the size of the voxels in the patient image. Figure 3.2 shows a schematic of this effect. The pixel values in the final image correspond to the average intensity over the entire voxel. The result of this is blurring in the image, especially for small features. The example in figure 3.2 shows a blood vessel that is

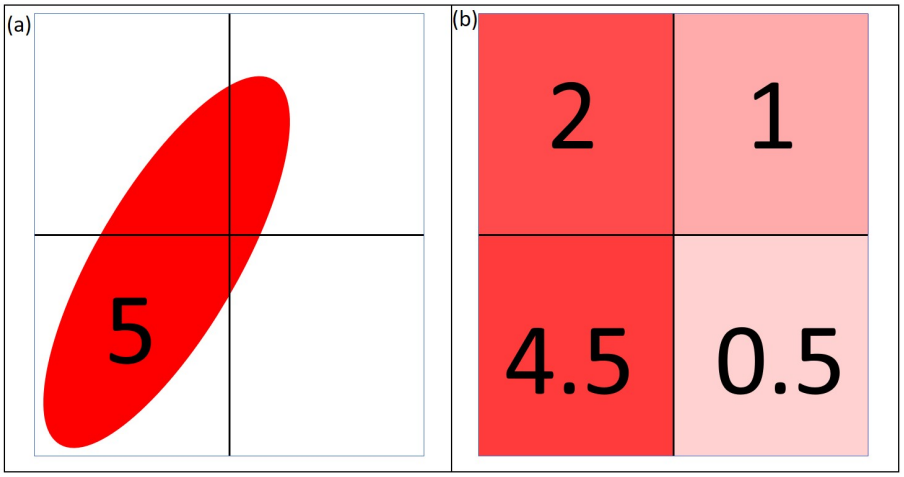

FIGURE 3.2: Diagram showing how the partial volume effect works. (a) Shows a small blood vessel with the pixel size of the detector overlaid. (b) Shows how the pixel values that would be associated with this vessel

mostly contained in the bottom left and top left pixels of the image. The partial-volume effect would blur this vessel over all four pixels. The two pixels on the right are more intense than they should be, while the two pixels on the left are less intense (Geus-Oei et al., 2006).

In addition to the partial volume effect and just like for automatic blood samples, image-derived input functions will have to be corrected for dispersion and delay. All these factors added together make these techniques more difficult to perform in a regular clinical setting.

3.1.7 Population-Based Input Functions

Population-based methods use existing data sets to estimate an input function. Thousands of input functions from different patients are averaged together to produce the final population-based input function. This type of averaging is only accurate if only the tail of the input function is used, as the tail tends to not differ significantly from person to person. Unfortunately, the fast-changing portion of the input function at the beginning of the scan varies greatly from person to person and is extremely important when performing kinetic modeling (Eberl et al., 1997). There is also the fact that this

technique cannot be used for novel tracers, as a sufficiently large data set is required to make the average. Furthermore, since the shape of the input function relies heavily on the biology of each individual, averaging a population data-set can mask important differences between patients (Eberl et al., 1997).

3.1.8 External Detectors

Another methodology to overcome the invasive blood sampling procedure is to use an external detector to measure the AIF. Different detector designs have been proposed over the years including scintillating detectors placed over the patient's neck and wrist and miniature PET detectors. (Watabe et al., 2001; Watabe et al., 1995; Kriplani et al., 2006; Kriplani et al., 2005; Villanueva et al., 2003) None of the proposed detectors are used clinically due to the high cost or low signal-to-noise ratio (SNR). The low SNR is due to the photons emitted from the patient's body that are detected along with the desired signal. The general concept behind such detectors is to use inorganic crystal scintillators to measure photon counts coming from the patient's wrist. The added background from the photons emitting from the rest of the body greatly increase the noise. Furthermore, the crystals used in such detectors are very costly, rendering the final product prohibitively expensive.

There is another plastic scintillating fiber based detector currently in development that shows good promise, but it is invasive and requires implantation of the fiber into the patient's vein. In addition, this detector relies on arterializing venous blood which is an additional step and is not suitable for all imaging modes (Knowland et al., 2018).

3.2 Design Considerations

To overcome the issues related to invasive blood sampling and the acquisition of the AIF, we have developed a non-invasive, scintillation-based, prototype positron detector, hereinafter called NID. Our detector relies on the relatively shallow placement of the radial artery in the patient's wrist ($1.99 \pm 0.99\,\mathrm{mm}$ (Lee et al., 2016)) and the range of positrons in tissue as seen in table 3.1. Note that the maximum range in tissue for the emitted positrons from PET radioisotopes are longer than the average skin to surface distance of the radial artery. This means that positrons escape the patient's wrist through the radial artery, and these positrons can then be detected. The NID measures the positrons emitting from the patient's wrist yielding the AIF.

While designing this detector, we kept several considerations in mind.

1. The detector should detect positrons in the energy range of 0-1 MeV but not detect 0.511 MeV annihilation photons.
2. The detector must detect positrons exciting a patient's wrist at clinically relevant activity concentrations.
3. The detector must be able to separate the positrons emitting from the patient's artery from the positrons emitting from the patient's veins and tissue.

These three factors were used to guide the design of the detector.

3.2.1 Consideration 1: Discriminating Against Photons

Positrons readily interact with electrons to produce a pair of 0.511 MeV photons. These photons are detected by PET scanners to produce PET images (Cherry, Sorenson, and Phelps, 2012). During a PET scan, these photons are constantly emitted from the entirety of the patient's body. Since the NID is detecting positrons, these photons are considered as noise and must be discriminated against. To do this, care was taken

in selecting a plastic scintillating fiber that has a small photon interaction probability. We use a 1 mm polystyrene core fiber (BCF-12, Saint-Gobain Crystals and Detectors, Paris, France). The interaction probability of a single 0.511 MeV photon while passing through 1 mm polystyrene is about 1% (NIST, 2019). Because of this low interaction probability, an assumption that all detected counts come from positron interactions is made.

3.2.2 Consideration 2: Clinically Relevant Activity Concentrations

To be of use in a clinical setting, the NID must be able to accurately detect the positrons escaping from the patient at clinically relevant activity concentrations. Geus-Oei *et. al.* (Geus-Oei et al., 2006) report peak human plasma activity concentrations in the 0.14 MBq/mL range, and Watabe *et. al.* (Watabe et al., 2006) report peak plasma activity concentrations above 1.1 MBq. These are the activity concentrations we should aim to detect. The methods and results section of this thesis describes in detail experiments that were performed to tests this.

3.2.3 Consideration 3: Background Rejection

The true AIF is the activity concentration in the arterial blood only. After the first pass of the bolus through the patient's wrist, the bolus will disperse through the patient's tissue and circulatory system. Kriplani *et. al.* demonstrated that pixel size on the order of 2 mm is enough to differentiate between tissue, artery and vein (Kriplani et al., 2006), hence this is what we aim to implement in the future. At this time, the NID does not perform background rejection.

3.2.4 Previous Measurements

All versions of the detector use BCF-12 plastic scintillating fibers (BCF-12, Saint-Gobain Crystals and Detectors, Paris, France) with a diameter of 1 mm. The physical properties of the fiber to determine its suitability for the NID's intended use were examined in a previous study (Turgeon, Kertzscher, and Enger, 2018). This series of experiments used a scintillating fiber that was looped one to five times around a positron emitting radioisotope. The work showed that there is a trade-off between the collection efficiency of the detector and the scintillating fiber length and radius of the loops. As the length of the fiber increased, and the radius of the loops decreased, the collection efficiency of the detector decreased. Conversely, increasing the length of the scintillator increases the available surface area for the positrons to interact within thus increasing the signal from the detector. However, there is a trade-off where it is desirable to both reduce the number of loops to decrease attenuation in the fiber and to increase the number of loops to increase the available surface area. This is an optimization problem that must be solved as all these factors will impact the detector's final efficiency.

Chapter 4

Methods

This chapter describes the construction of the NID and the experimental procedure used to validate it against a microfluidic detector. Two separate experiments were performed using similar, but different detector designs and experimental setups. In both experiments, the NID was tested against a microfluidic detector used in small animal PET studies, which was previously validated by (Convert et al., 2011). This detector receives input from small diameter tubing, has a sensitive volume of 0.9 μl, and uses PIN photodiodes to detect positrons emitting from the radioisotope. Due to the very thin-walled tubing that was used, and the minimal amount of attenuating material in the detector, this detector will detect almost every emitted positron. As such, the microfluidic detector is used as the ground truth for these studies.

TABLE 4.1: Properties of scintillating and transmission fibers. Data obtained from the Saint-Gobain and ESKA.

Characteristic	**BCF-12**	**Eska GH4001**
Core material	Polystyrene	PMMA
Core density	1.05 $\mathrm{g/cm^3}$	1.2 $\mathrm{g/cm^3}$
Core refractive index	1.60	1.49
Cladding material	PMMA	Fluorinated Polymer
Cladding refractive index	1.49	N/A
Diameter, with cladding	1.00 $\pm$ 0.02 mm	1.000 mm
Numerical aperture	0.74	0.5
1/e attenuation length	270 cm	5101 cm
Emission peak	435 nm	-
Scintillation decay time	3.2 ns	-
# of photons / MeV	$\approx$ 8000	-

4.1 Experiment 1

4.1.1 Detector Design

In the performed experiments 300 cm of BCF-12 scintillator was used. First, the scintillator was placed inside a 7.2 μm thick heat shrink tubing (Vention Medical, USA) for protection and both ends of the fiber were polished using increasingly fine polishing paper (LF6D, LF3D, LD1D, LFCF, ThorLabs) to remove any visible scratches. This is done to prevent signal loss from photons scattering off the scratches. Both ends of the fiber were then coupled to 5 m of transmission fiber with a poly-methyl-methacrylate (PMMA) core (Eska-GH4001, Mitsubishi Chemical, Japan). The coupling was performed using a UV cured optical glue (NOA68, Norland, United-States). The coupling joints represent weak points in the detector and can easily break under mechanical stress. To prevent this, a 6 cm plastic tube was placed over each joint and was filled with epoxy. The epoxy lends some rigidity to the joints. SMA style connectors (SMA905, ThorLabs) were then affixed on the uncoupled ends of the transmission fibers.

A 3D printed polylactic acid (PLA) sheath was then used to contain the fiber where it was looped in 10 5 cm radius loops. This geometry was chosen for its ease of use when performing experiments and provides sufficient signal for detector validation. Figure 4.1 shows the 3D model of the printed sheath.

Detailed characteristics of the scintillating and transmission fibers can be found in table 4.1. The terminated transmission fibers are each connected to a PMT (H6779, Hamamatsu, Japan). The PMT was chosen so that its peak efficiency is matched with the peak emission wavelength of 435 nm of the scintillating fiber. The PMTs were read-out without amplification using an oscilloscope (SO-X 2012A, Keysight) controlled by Matlab. The oscilloscope was setup to acquire 5 ms waveforms at a rate of 2.87 waveforms per second.

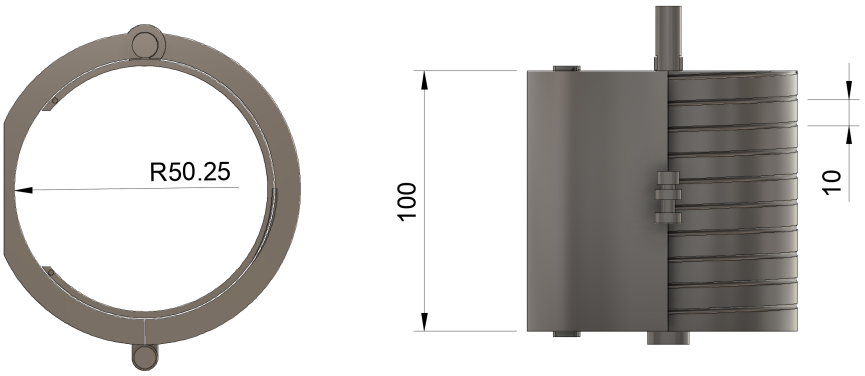

FIGURE 4.1: 3D model of printed sheath for experiment 1. All units are in mm.

4.1.2 Experimental Setup

The NID was placed in a light-tight box with the transmission cables leading out behind a shielded wall where the PMTs and oscilloscope were located. A cylindrical polyethylene (density 0.9 g/cm^3) phantom was used to simulate a patient's wrist and can be seen in figure 4.2. The phantom's diameter was 6.41 cm, and a hole with diameter of 3.25 mm was drilled at a depth of 2 mm to mimic the radial artery. This phantom was validated in a previous study(Turgeon, Kertzscher, and Enger, 2018). For this experiment, the phantom was placed inside the PLA sheath at the same location where a patient would place their arm.

A polyethylene tube (PE50) with 0.53 mm inner diameter and 0.965 mm outer diameter was passed through the hole in the phantom so that it passed through the entire detector. This tube was used to create a closed loop going from a liquid reservoir, through the phantom, to the microfluidic detector, through a microfluidic pump and back to the reservoir. A light proof cloth was placed over the top of the box that contained the NID. Figure 4.3 shows a schematic of the experimental setup. The liquid reservoir consisted of a beaker that was placed on a mixing plate filled with water. Radiation was injected into the system by use of a syringe that expelled the radiation into the liquid reservoir.

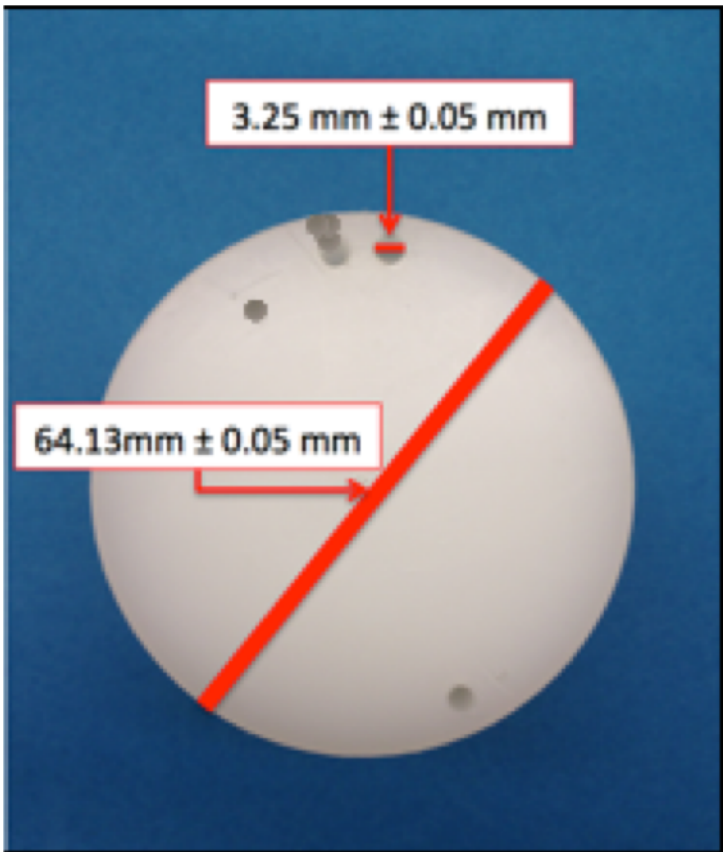

FIGURE 4.2: Dimensions of the polyethylene wrist phantom

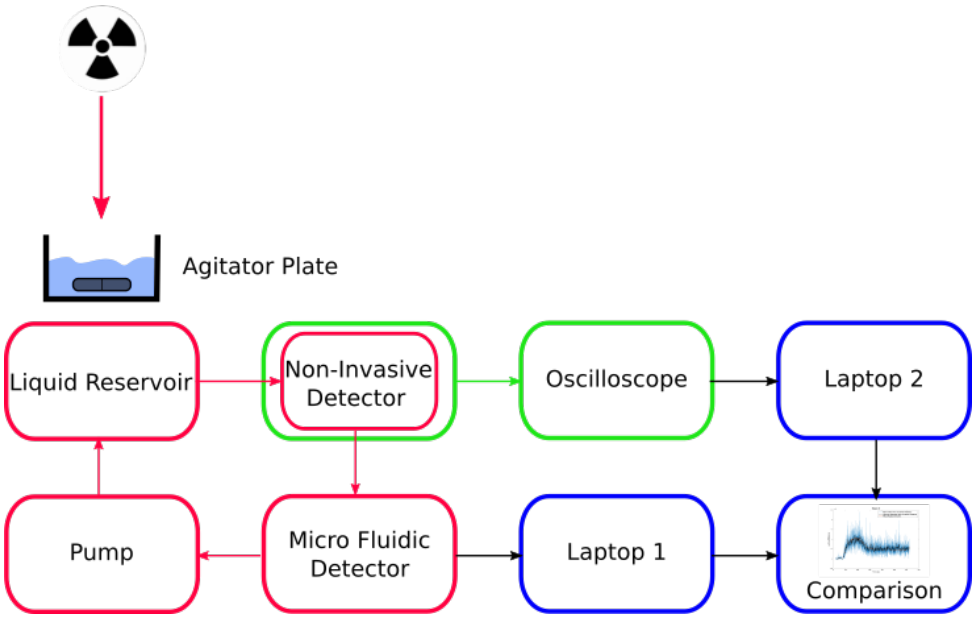

FIGURE 4.3: Schematic of the acquisition setup used for the first set of measurements.

A total of three scans were performed using three different radioisotopes: ^{18}F, ^{11}C and ^{68}Ga. Half-life, average and maximum energy, and average and maximum range in

water of positrons emitted by these three radioisotopes are presented in table 3.1. Each scan began with 30 seconds of water circulation followed by an instantaneous injection of the radioisotope to produce a sharp measurable peak. Two minutes after injection, 6 mL of water was added over the course of one minute. This was to mimic the clearance of the radioisotope as the bolus disperses through the human body. Total scan duration was 10 minutes. Table 4.2 lists the scan parameters. Each waveform collected from the oscilloscope was averaged to produce one data point which were then plotted over time. The SNR was calculated by taking the mean of the points lying between the full-width half maximum of the peak and dividing by the standard deviation of the first 30 seconds of the scan. The resulting data set was smoothed by using a 5 point moving average filter. The data from the NID was then normalized to the data collected from the microfluidic detector and the two detectors were then compared.

Scan Number	Used	Activity (MBq)	Wash Volume (mL)	Injection Volume (mL)
1	^{18}F	22.8	6	0.3
2	^{11}C	48.4	6	0.3
3	^{68}Ga	38.4	6	0.3

TABLE 4.2: Scan parameters for experiment 1. The wash volume is the volume of water used to wash out the tracer in the experiment. The injection volume is the volume of radiotracer in which the Activity was diluted.

4.2 Experiment 2

4.2.1 Detector Design

2.8 m of single-clad BCF-12 scintillating fiber with a 1 mm diameter was enclosed by the same heat-shrink tubing as described in experiment 1. The same polishing process was performed at each end of the fiber. Each end of the scintillator was coupled to a silicon photo-multiplier (SiPM) (MicroFC-SMA-10020, SensL, Irelande) using optical coupling silicon grease (BC-630, Saint-Gobain Crystals and Detectors, Paris, Franc). SiPMs were chosen for their robustness and superior timing performance when compared to

traditional PMTs (Knowland et al., 2018; Moon et al., 2016). In addition, they can be used in strong magnetic fields, such as those present in PET/MRI multi-modal imaging (Bailey et al., 2018; Wagenknecht et al., 2013; Ehman et al., 2017; Herzog and Lerche, 2016) while PMTs cannot. They are also less expensive than PMTs. The chosen SiPM was selected to match the emissions from the BCF-12 scintillating fiber and produce pulses with a rise time on the order of 20 ns. These pulses will be amplified 100x (by two low noise amplifiers (ZFL-1000LN+, minicircutis, USA) and read out by a desk-top digitizer capable of reaching nanosecond timing resolution (DT5730, CAENS.p.A., Italy) to produce fine time stamps and filter out noise. The chosen digitizer is also capable of coincidence detection. Since the proposed detector is dual-readout, each channel can be read by a separate digitizer channel and a coincidence time window can be set to remove the SiPM dark counts and other noise.

The scintillating fiber was wrapped around a 3D printed PLA sheath depicted in figure 4.4. The sheath held the fiber in a coil with 16 loops each with a radius of 2.5 cm. The fiber and both SiPMs were placed inside a light tight box.

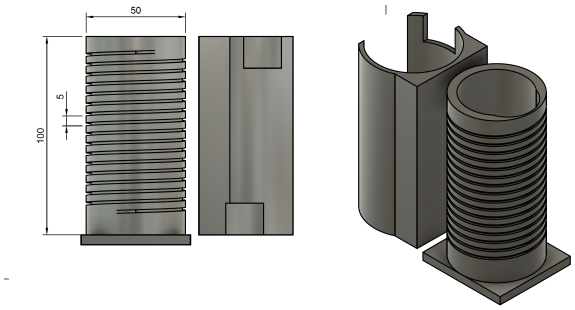

FIGURE 4.4: 3D model of printed for second experiment

4.2.2 Experimental Setup

As in experiment 1, a PE50 tubing closed loop circuit was setup going from a liquid reservoir, through the phantom, to the microfluidic detector, through a microfluidic pump and back to the reservoir. The SiPMs in the NID were biased to +28 V by an external power supply. Three scans were performed one with ^{18}F and two with ^{11}C.

The scans began with 30 seconds of water circulation followed by an instantaneous injection of the radioisotope to produce a sharp measurable peak. Two minutes after injection, 2 mL of water was added over the course of one minute. This was to mimic the clearance of the radioisotope. Total scan duration was 10 minutes. Table 4.3 lists the scan parameters.

Scan Number	Isotope	Activity (MBq)	Wash Volume (mL)	Injection Volume (mL)
4	^{18}F	40	2	0.2
5	^{11}C	40	2	0.2
6	^{11}C	40	2	0.2

TABLE 4.3: Scan parameters for experiment 2. The wash volume is the volume of water used to wash out the tracer in the experiment. The injection volume is the volume of radiotracer in which the Activity was diluted.

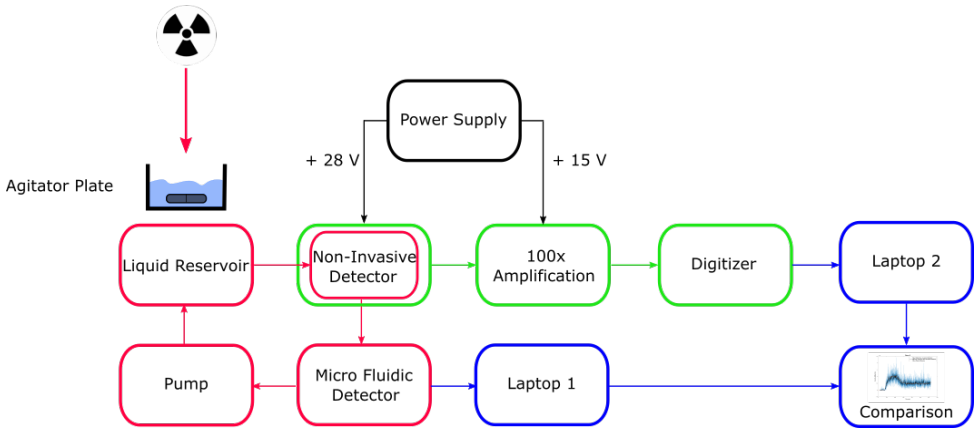

FIGURE 4.5: Schematic of the acquisition setup used for the second set of measurements.

The data from the NID was amplified 100x and then sent to the desktop digitizer. The digitizer used a field programmable gate array (FPGA) and digital pulse processing (DPP) firmware to emulate a constant fraction discriminator (CFD) followed by a charge integrating analog to digital converter (QDC). The CFD discriminated against pulses below a certain threshold. This allowed the setup to reject pulses due to the SiPM dark counts which count as noise. Secondly, the CFD measured the time of arrival of each pulse. The QDC integrated the voltage of the pulses that passed the CFD and digitized the signal. Scan 6 differs from the other scans in that a 50 ns coincidence window was put in place between both channels. This window only accepts pairs of

pulses that arrive at both channels within 50 ns. Each pulse was given a time tag and an energy tag before being saved on a connected computer. The data from each channel was then binned into 1 second bins and normalized to the data obtained from the microfluidic detector by matching the FWHM of the peaks. The two data sets were then compared.

The SNR was calculated by taking the mean of the points lying between the full-width half maximum of the peak and dividing by the standard deviation of the first 30 seconds of the scan. A linear regression was performed comparing the results from the two detectors.

Chapter 5

Results

5.1 Experiment 1

Table 5.1 shows the SNRs and maximum concentrations for the three scans. This detector is designed to be used with human patients who have an average radial artery diameter of 2.2 mm (Lee et al., 2016) which is in contrast to the tubing used in this study, with an inner diameter of 0.53 mm. There is a 17.23 times increase in volume between the average patient's radial artery for the same length of tubing used for this study and hence an equivalent decrease in the activity concentration. Table 5.1 shows the equivalent activity concentration if the same total activity was used in a human artery. This table also shows the SNRs for the first 3 scans.

Scan Number	SNR	Peak Activity Concentration (MBq/mL)	Equivalent Activity Concentration (MBq/mL)
1	5.16	5.6	0.32
2	22.16	13.4	0.78
3	15.38	10.3	0.60

TABLE 5.1: NID SNRs. Maximum concentration measured by the microfluidic detector and corrected for blood volume of the radial artery.

Figure 5.1 shows a comparison between the results obtained from the NID and the microfluidic detector. All three scans are represented in this figure. The results from the NID are shown in red. No smoothing filter was applied and the results were not decay corrected. The microfluidic detector results are shown in black. These results are

smoothed by the post-processing software controlling the output of the device and the results are corrected based on the radiotracer to take into account lost counts due to positron scattering and attenuation. The NID was able to detect the sharp peak as the bolus passed through the system and follow the gradual activity concentration fall off. Note that the radiotracer was passed through the wrist phantom for these experiments. The phantom attenuated the positrons in the same manner as the patient's wrist would. As such, these graphs are representative of the NID's performance in a clinical setting. Note the difference in scale on the y-axis for scan 2 when compared to scans 1 and 3.

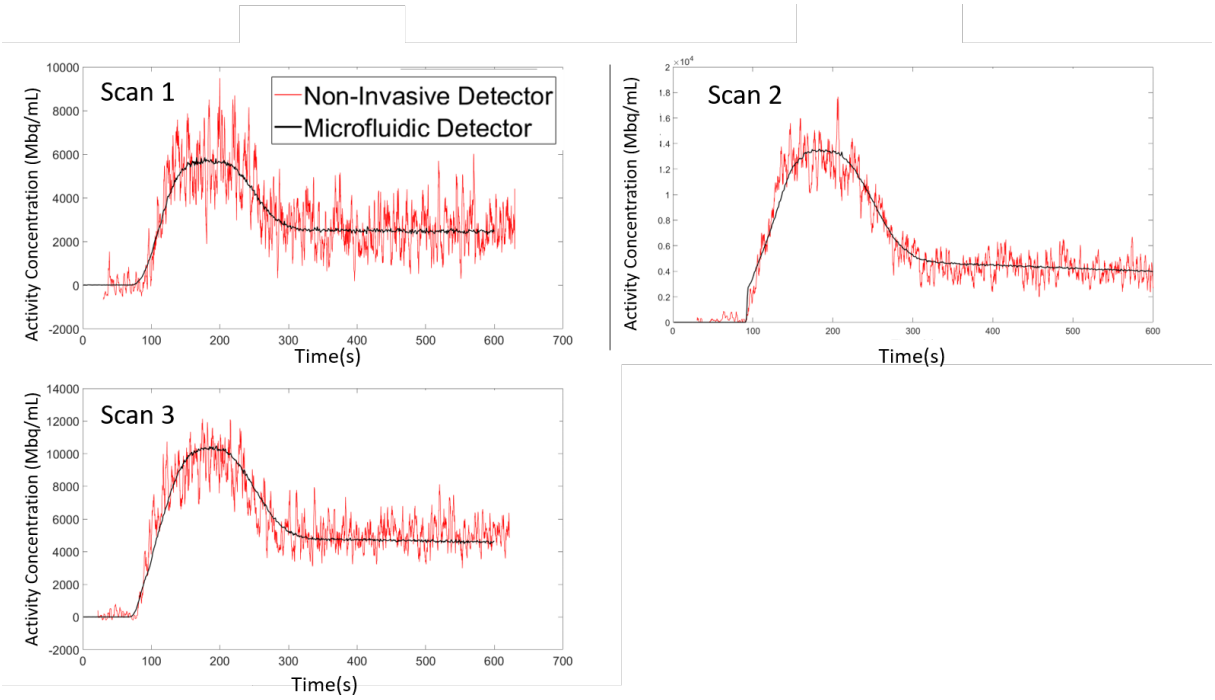

FIGURE 5.1: Results from experiment 1 showing the measured input functions for scans 1, 2 and 3.

5.1.1 Experiment 2

Figure 5.2 shows the measured data and linear regressions for scans 4-6. On the left for each scan, the red line shows the NID results while the black line shows the microfluidic detector results. While all three NID curves were able to match the microfluidic detector results, scan 4 showed considerable noise as seen in table 5.2. This can also be seen in the linear regressions on the right side of the figure. The slope, intercept and

R^2 values for the regresssions can be seen in table 5.3. Figure 5.3 compares channel one and channel two of the NID during scan 5. Note that channel two recorded less than a third of the counts as channel one.

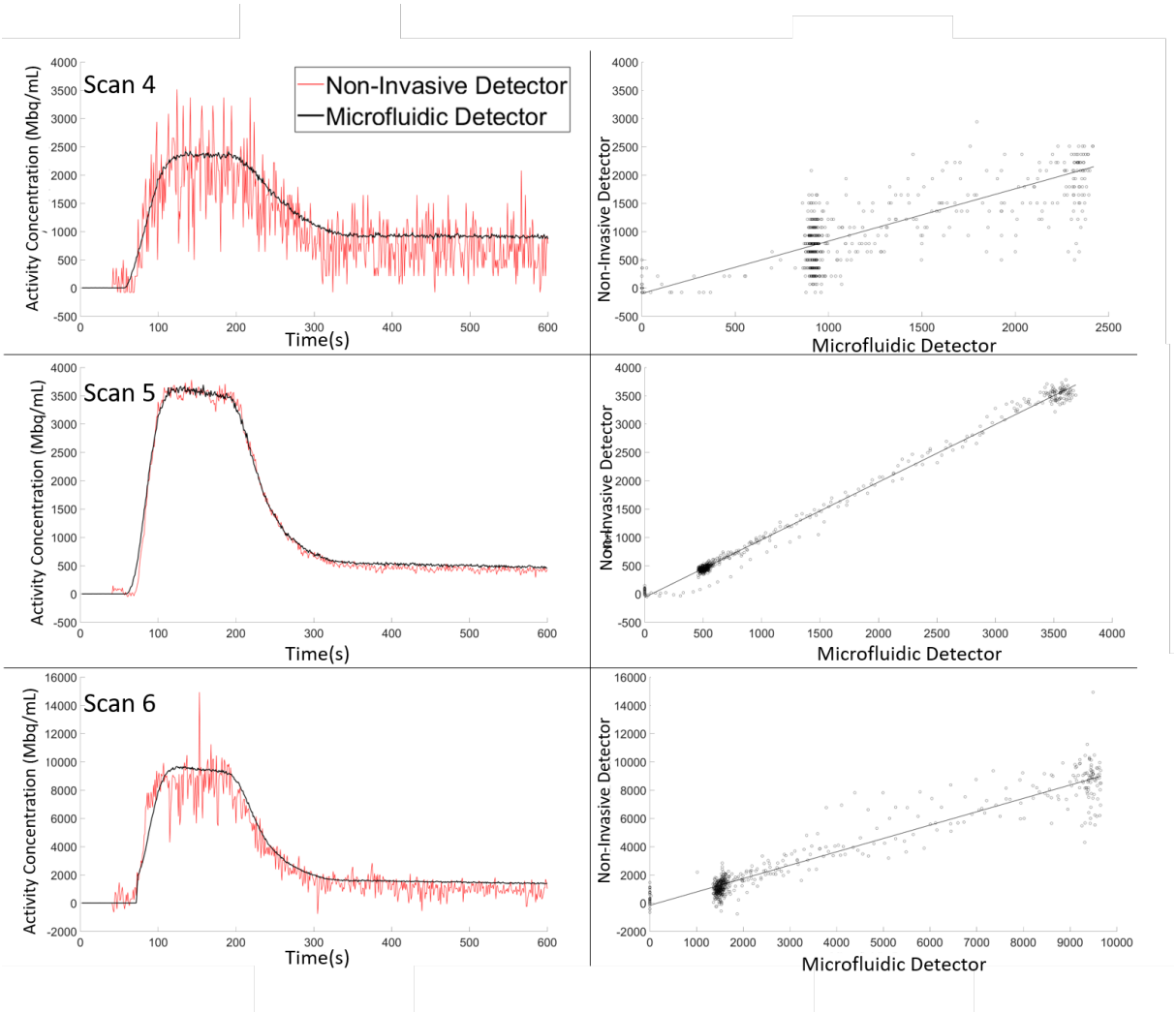

FIGURE 5.2: Results from experiment 2 showing the measured input functions and linear regressions for scans 4, 5 and 6.

Because of the coincidence logic employed during scan 6, it has more noise than in scan 5.

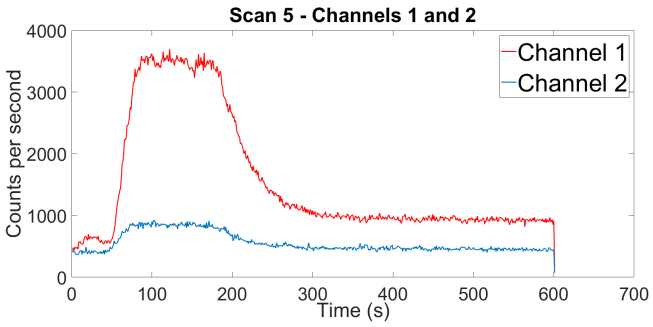

FIGURE 5.3: Comparison between both channels of the NID during scan 6. Similar results were seen for scans 4 and 5.

Scan Number	SNR	Peak Activity Concentration (MBq/mL)	Equivalent Activity Concentration (MBq/mL)
4	17.80	2.42	0.14
5	52.18	3.69	0.21
6	14.75	9.67	0.56

TABLE 5.2: NID SNRs. Maximum concentration measured by the microfluidic detector and corrected for blood volume of the human radial human artery for the second experiment

Scan Number	Slope	Intercept	R^2
4	0.93	-96.74	0.68
5	1.02	-60.04	0.99
6	0.94	-156.13	0.92

TABLE 5.3: Results from the linear regression.

Chapter 6

Discussion

6.0.1 Detector Motivation

Kinetic modeling of dPET data sets has a variety of uses, including diagnosing and staging cancer (Takesh, 2012; Thorwarth et al., 2005), diagnosing neuro-degenerative disorders (Baker et al., 2017) and characterization of new pharmaceutical drugs (Tucker et al., 2018). Unfortunately, widespread clinical adoption of this technique is limited due to the difficult clinical workflow, when compared to static PET, due to the invasive acquisition of the AIF (Kotasidis, Tsoumpas, and Rahmim, 2014). To remedy this issue, several non-invasive methods to acquire the AIF have been developed including novel detectors and various post-processing methodologies (Litton and Eriksson, 1990; Watabe et al., 2001; Knowland et al., 2018; Geus-Oei et al., 2006; Eberl et al., 1997). All current solutions have limitations. We have designed a non-invasive positron detector that is capable of measuring the arterial activity concentration of a patient, and have validated it against an invasive microfluidic detector using clinically relevant activity concentrations. This detector will have applications both in a research environment and in the clinic.

Previous non-invasive designs used large blocks of scintillators to detect photons (Kriplani et al., 2006; Watabe et al., 2001). During any PET scan, there will be high energy photons emitting from all parts of the patient's body which will readily interact in the large block scinitillators adding noise to the signal. This adds additional complications,

in the form of shielding requirements, to the design of the detector. Our detector uses scintillators that are 1 mm in diameter so as to interact with a very small fraction of the emitted photons, but can easily detect the positrons that escape the patient's wrist, as shown in a previous study with this detector design (Turgeon, Kertzscher, and Enger, 2018).

Current invasive methods require catheter insertion into the patient's artery to draw blood. Use of the NID will simplify acquisition of dPET data sets. During the scan, the NID will constantly monitor the activity levels in the radial artery. At the end of the scan, a single venous blood sample will need to be drawn from the patient to be used to calibrate the data set from the NID. This blood sampling is much less invasive than current automatic blood samplers and other detectors in development (Knowland et al., 2018).

6.1 Detector Design

The NID went through several design iterations before the version used in these experiments was developed. The first prototype that had a 3D printed sheath to contain the scintillating fibers used 3 meters of fiber held in loops with a 15 cm radius. Figure 6.1 shows the design of this first sheath. Grooves on the inside of the sheath housed the fiber which had to be passed through small holes on the outside. Finally, a cover held everything in place and protected the fibers, leaving a window where the patient would place their wrist.

Unfortunately, this design was impractical for two reasons. Firstly, it was extremely difficult and time consuming to weave the scintillating fiber into the sheath. The increased handling also increased the chance of damaging the fragile fibers. The second concern is clinical usability. Due to the large size of the detector, holding it over the patient's wrist would be extremely difficult. One of our clinical advisers, Dr. Mark Lubberink, advised us that the detector would be too bulky for certain arm positions

that patients hold during a dPET scan. Figure 6.2 shows how a patient would place their wrist in the sheath.

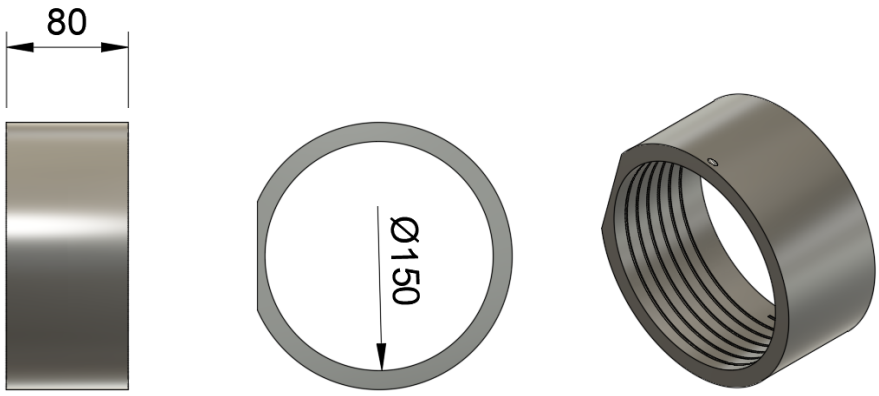

FIGURE 6.1: Schematic showing the first 3D-printed sheath used to house the scintillating fiber. All units are in cm.

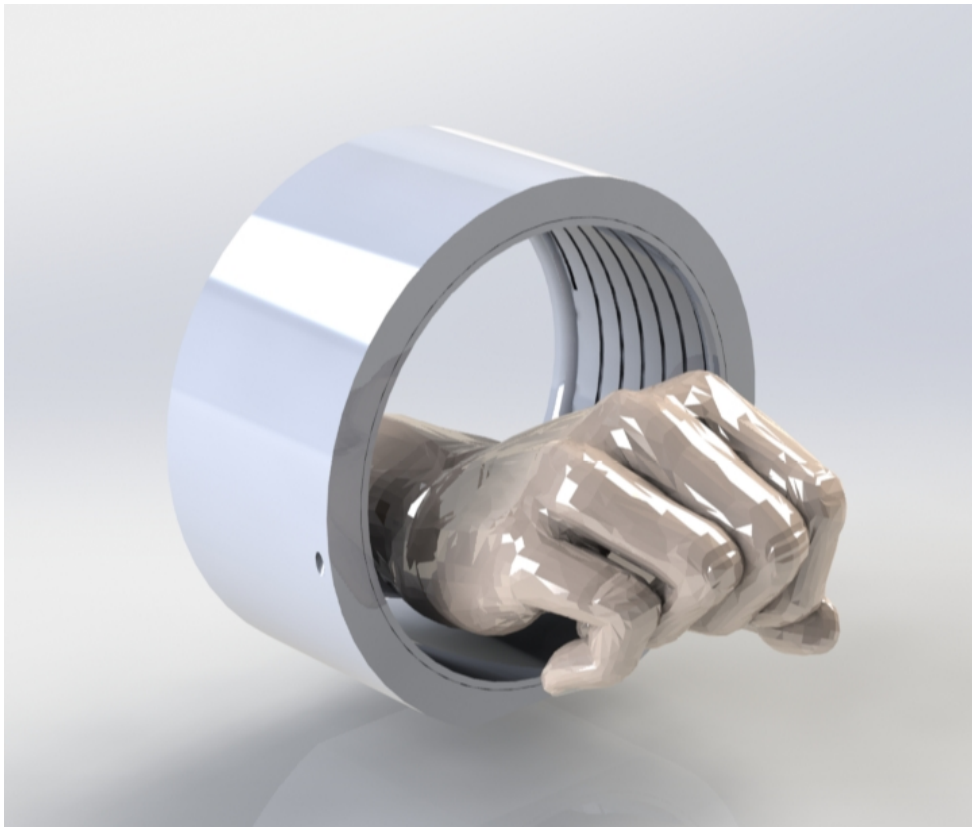

FIGURE 6.2: Graphic showing the placement of a patient's arm through the sheath

The second version of the detector used the sheath seen in figure 4.1. This is the same sheath design that was used in experiment 1, but other parts of the detector differ. The 10 cm radius is still large enough to prevent too much signal loss and allows for ten fiber loops to get more surface area in contact with the patient's wrist. The improved design of this sheath allowed for a much quicker and easier loading of the scintillating fiber. The smaller design of the sheath allowed for easier placement of the patient's wrist. Finally, a light-proof bag is placed over the sheath and the patient's arm to prevent ambient light from adding to the detector noise.

Initial tests with this design revealed one key flaw: high energy positrons passing through the air could interact with the scintillating fiber and mask the true signal. Since the radio-isotope is injected into the patient's arm, there is a period of time where it flows through a very thin-walled plastic tube before entering into the patient. At this time, the radiotracer is highly concentrated and is emitting positrons that can pass through several meters of air (Alexoff et al., 2011) and interact with the NID. This would create a large spike in the data set, masking the first seconds of true data.

To get around this issue, the third version of the detector used a light-tight box with water equivalent attenuating material to block outside positrons. Looking at table 3.1, it only takes a couple of millimeters of water equivalent material to attenuate the majority of positrons that would be emitted during a dPET scan. This is the version of the detector that was described in the methods section of experiment 1.

The final version of the detector used for this research is the version used in experiment 2. The same light-tight box was used as in experiment 1, but with a different 3D-printed sheath shown in figure 4.4. This insert used a smaller radius of 2.5 cm which allowed for additional loops. The design of this sheath allowed the patient to rest their wrist on its outside. Unfortunately, the small radius size of the scintillating fiber attenuated the signal too much. Future versions of the detector will move back to a larger loop radius.

6.2 Experiment 1

Tables 5.1 presents results obtained for experiments performed in the first part of the study. The activity concentrations used were greater than those normally found in a clinical dPET scan, however, the volume of the PE50 tubing is much smaller than the volume in the average radial artery. If the same total activity was dispersed in a tube the size of a patient's artery, the activity concentration would be seen to be clinically relevent for humans. Geus-Oei *et. al.* report peak human plasma activity concentrations in the 0.14 MBq/mL range(Geus-Oei et al., 2006), and Watabe *et. al.* report peak plasma activity concentrations above 1.1 MBq/mL (Watabe et al., 2001). The equivalent concentrations for all scans fall within the range presented by these publications with lowest being scan 1 with 0.32 MBq/mL and the highest being scan 2 with 0.78 MBq/mL. Furthermore, due to the higher activity used in animal studies, as shown in Tucker *et. al.* who report peak activity concentrations up to 2 MBq/mL in rabbits (Tucker et al., 2018), this detector could also be used for animal studies. In fact, the higher activity concentrations will only improve the SNR of the NID when used with animal studies.

The first set of measurements, as seen in figure 5.1, were used as a proof of concept for this detector. The NID was able to replicate the general shape of the input function recorded by the microfluidic detector. The relatively low SNRs of 5.16, 22.16 and 15.38, for scans 1-3 respectively, are in part due to the use of an oscilloscope as a read-out device instead of dedicated electronics. The oscilloscope recorded 5 ms of waveform 2.87 times per second. This means that the duty cycle of the detector was only 1.43 % and that more than 98 % of the time, the detector was not recording data. To make matters worse, the detector was not able to discriminate against background noise and dark counts from the PMTs. The 5 ms waveforms were averaged together to get a single timepoint, which included the noise and dark counts. To try and remove the unwanted data, 30 s of background was acquired at the beginning of each scan which was then subtracted from the final data sets. Due to the preliminary nature of the

results, they were not analyzed further. Instead, the second set of experiments were designed to improve the SNR of the detector.

6.3 Experiment 2

With the addition of the SiPM, digitizer and amplifiers to the detector design, the results from experiment 2 show a large improvement over experiment 1. Scan 5 in figure 5.2 shows that the NID very closely matches the input function from the microfluidic detector. This is also evident from the linear regresssion results which yielded a slope of 1.02 for scan 5 with an R^2 of 0.99. In this regression plot, there are several points below the fit. This is due to the sharper, but delayed rise seen by the NID when compared to the microfluidic detector. This difference in rise time is due to the fact that the NID was placed before the microfluidic detector in the experimental setup. The dispersion effect described earlier would cause the bolus to disperse as it travels through the PE50 tubing. The end result of this is that the bolus will be more spread out when it reaches the microfluidic detector leading to a longer rise time as observed in figure 5.2.

The other two scans in figure 5.2 are much noisier due to lower number of counts per second. Scan 4 used ^{18}F, which emits a positron with a much lower maximum energy, as seen in table 3.1. Due to the lower maximum and average energy, fewer positrons were able to escape the wrist phantom leading to fewer counts in the detector. This can be improved upon by increasing the bending radius and decreasing the number of loops in the scintillating fiber. This will reduce the signal loss as the scintillating photons travel through the fibers. Another method to improve upon this is to increase the surface area of the scintillator in contact with the phantom. This will increase the number of positrons incident on the detector and thus increase the counts per second.

Scan 6 had a different problem, arising from the fact that it was the only scan where coincidence logic was used. The logic is simple and takes advantage of the dual-readout nature of the NID. When a positron deposits energy in the scintillator, photons are

emitted isotropically in the fiber. This results in photons going towards both light sensors. The coincidence logic is implemented so that a count from one light sensor will only be accepted if there is another count in the opposite light sensor in a 50 ns time window. This is done to reduce the number of dark counts from the SiPMs that get recorded. Since the dark counts are randomly dispersed in time, there is a very low chance that both SiPMs see a dark count in a 50 ns interval. The unwanted side-effect of this is that if a true event occurs and the photons make it to one SiPM but not the other, then the count will be lost. This is possible due to the attenuation of the photon packet as it travels through the scintillating fiber, and is part of the reason why scan 6 had such a lower SNR. The other reason for the low SNR is best seen through figure 5.3.

Figure 5.3 shows both channels of scan 5 and it is very apparent that channel 1 collected many more counts that channel 2. This is most likely due to inefficient coupling between the SiPM and the scintillating fiber during the second experiment. A second explanation would be a break in the scintillating fiber near the channel 2 end which would greatly attenuate any signal passing through it. Due to this large difference in signal, many true events would be rejected using the coincidence logic described above. This can be seen by comparing scan 5 to scan 6 in figure 5.2. Both scans used the same setup, the only difference being scan 6 employed the coincidence logic. This resulted in a much lower SNR, 14.75 compared to 52.18, and a worse linear fit.

6.4 Future Work

One consideration that has not yet been addressed is the spatial resolution of the detector. The true AIF is the activity concentration in the arterial blood only. After the first pass of the bolus through the patient's wrist, it will disperse through the patient's tissue and circulatory system. As mentioned earlier, a pixel size on the order of 2 mm is sufficient to differentiate between tissue, artery and vein (Kriplani et al., 2006). The

dual readout system enables the determination of the point along the fiber where a scintillation event occurs. This can be accomplished by measuring the difference in arrival times between the pulses arriving at the two PMTs from the same event. We can determine the theoretical resolution of such a setup as follows: From the refractive index of the scintillator, we can calculate the theoretical speed of light through the plastic (eqn 6.1).

$$v = \frac{c}{n} = \frac{c}{1.60} = 1.87 * 10^8 \ \frac{m}{s} \tag{6.1}$$

By measuring the time difference between two measurements (Δt), we can calculate the difference in path lengths that the two signals travelled (Δx). The precision to which we can calculate Δx depends on the precision of the Δt measurement. To achieve a Δx resolution of 31 cm, a Δt resolution of 1.6 ns is required. This is quite feasible with modern electronics(Di Francesco et al., 2016). While a 31 cm resolution is not particularly useful, by looping the scintillating fiber around the patient's wrist in 10 cm loops, we can increase the path length to 31 cm per loop of fiber and then the size of the fiber becomes the limit on the resolution. As the current fiber is 1 mm in diameter, this is the current theoretical resolution of the detector. The achievable spatial resolution will be tested in a future study.

Chapter 7

Conclusion

This thesis covered the mechanisms of interactions of light charged particles and uncharged particles in scintillators. Following this, a detailed explanation of the mechanism of action of plastic organic scintillators was presented detailing the process of scintillation as well as the components of a typical plastic scintillator. Further discussions on the nature of scintillating fibers and their components followed. Finally, two read-out options for the scintillators were presented: photo-multiplier tubes and silicon photo-multipliers.

The objective of this thesis was to present the work done to validate a novel prototype of a non-invasive positron detector to measure the input function during dPET scans. This detector uses a dual-readout system to detect the interaction location and time of positrons escaping from the patient's wrist. This work is motivated by the clinical need to detect cancer treatment efficacy. Current standards to do this are slow and, sometimes inaccurate. dPET is a more accurate way to perform these measurements and can yield results earlier in the treatment cycle. This is all possible thanks to the use of kinetic modelling, which is a mathematical tool used to reconstruct the data from dPET scans. Unfortunately, this technique requires the AIF and all current methods to acquire it have downsides. The NID is designed to facilitate the adoption of dPET in oncology clinics, without the need for other specialized equipment or staff.

The detector was validated against an existing invasive blood sampling detector. We

showed that both detectors have comparable accuracy at clinically relevant activity concentrations and while the NID was detecting positrons through a phantom mimicking a patient's wrist. The NID will enable kinetic modelling to be performed with a simplified non-invasive workflow. Further measurements will be performed to fully characterize and optimize the detector. This includes measuring the detection efficiency and achievable spatial resolution of the detector as well as determining the optimal geometry (loop radius and pitch of the scintillator fiber) of the detector. Further improvements on the detector will drastically increase the total efficiency of the NID. Multiple fibers will be used instead of a single fiber in order to minimize signal loss due to scintillation photon attenuation and, the coupling between the fibers and the SiPM will be improved to reduce the signal loss at the coupling. With these improvements, the detector will be at a stage where it can be tested on patients. In this way, the results from the NID will be tested against the current gold-standard of blood sampling.

Bibliography

Alexoff, David L et al. (2011). "PET imaging of thin objects: measuring the effects of positron range and partial-volume averaging in the leaf of Nicotiana tabacum". In: *Nuclear medicine and biology* 38.2, pp. 191–200.

Bailey, D. L. et al. (2018). "Combined PET/MRI: Global Warming-Summary Report of the 6th International Workshop on PET/MRI, March 27-29, 2017, Tubingen, Germany". English. In: *MOLECULAR IMAGING AND BIOLOGY* 20.1, 4–20. ISSN: 1536-1632. DOI: {10.1007/s11307-017-1123-5}.

Baker, Suzanne L et al. (2017). "Reference Tissue-Based Kinetic Evaluation of 18F-AV-1451 for Tau Imaging." In: *Journal of nuclear medicine : official publication, Society of Nuclear Medicine* 58.2, pp. 332–338. ISSN: 1535-5667. DOI: 10.2967/jnumed.116.175273. URL: http://www.ncbi.nlm.nih.gov/pubmed/27587706http://www.pubmedcentral.nih.gov/articlerender.fcgi?artid=PMC5288744.

Bentourkia, M'hamed and Habib Zaidi (2007). "Tracer Kinetic Modeling in PET". In: *PET Clinics* 2.2, pp. 267–277. ISSN: 15568598. DOI: 10.1016/j.cpet.2007.08.003. URL: http://linkinghub.elsevier.com/retrieve/pii/S1556859807000211.

Birks, JB and FWK Firk (1965). "The theory and practice of scintillation counting". In: *Physics Today* 18, p. 60.

Boellaard, Ronald et al. (2001). "Characteristics of a new fully programmable blood sampling device for monitoring blood radioactivity during PET". In: *European Journal of Nuclear Medicine* 28.1, pp. 81–89. ISSN: 0340-6997. DOI: 10.1007/s002590000405. URL: http://link.springer.com/10.1007/s002590000405.

Champion, C and C Le Loirec (2007). "Positron follow-up in liquid water: II. Spatial and energetic study for the most important radioisotopes used in PET". In: *Physics*

in Medicine and Biology 52.22, pp. 6605–6625. ISSN: 00319155. DOI: 10.1088/0031-9155/52/22/004. URL: http://stacks.iop.org/0031-9155/52/i=22/a=004?key=crossref.1daf17f2e1836466fb122a3a39da746d.

Cherry, Simon R., James A. Sorenson, and Phelps (2012). "Interaction Radiation Matter". In: *Physics in Nuclear Medicine*. Elsevier, pp. 63–85. ISBN: 9781416051985. DOI: 10.1016/B978-1-4160-5198-5.00006-X. URL: http://linkinghub.elsevier.com/retrieve/pii/B978141605198500006X.

Convert, Laurence et al. (2011). "High efficiency microfluidic beta detector for pharmacokinetic studies in small animals". In: *Nuclear Instruments and Methods in Physics Research Section A: Accelerators, Spectrometers, Detectors and Associated Equipment* 652.1, pp. 735–738. ISSN: 0168-9002. DOI: 10.1016/J.NIMA.2010.09.111. URL: https://www-sciencedirect-com.proxy3.library.mcgill.ca/science/article/pii/S0168900210021443.

Di Francesco, Agostino et al. (2016). "TOFPET 2: A high-performance circuit for PET time-of-flight". In: *Nuclear Instruments and Methods in Physics Research Section A: Accelerators, Spectrometers, Detectors and Associated Equipment* 824, pp. 194–195. ISSN: 0168-9002. DOI: 10.1016/J.NIMA.2015.11.036. URL: https://www-sciencedirect-com.proxy3.library.mcgill.ca/science/article/pii/S0168900215014011?via{\%}3Dihub.

Driessen, Roel S. et al. (2017). "Myocardial perfusion imaging with PET". In: *The International Journal of Cardiovascular Imaging* 33.7, pp. 1021–1031. ISSN: 1569-5794. DOI: 10.1007/s10554-017-1084-4. URL: http://link.springer.com/10.1007/s10554-017-1084-4.

Eberl, Stefan et al. (1997). "Evaluation of two population-based input functions for quantitative neurological FDG PET studies". In: *European Journal of Nuclear Medicine* 24.3, pp. 299–304. ISSN: 0340-6997. DOI: 10.1007/BF01728767. URL: http://link.springer.com/10.1007/BF01728767.

Ehman, Eric C. et al. (2017). "PET/MRI: Where Might It Replace PET/CT?" English. In: *JOURNAL OF MAGNETIC RESONANCE IMAGING* 46.5, 1247+. ISSN: 1053-1807. DOI: {10.1002/jmri.25711}.

Eisenhauer, Elizabeth A et al. (2009). "New response evaluation criteria in solid tumours: revised RECIST guideline (version 1.1)". In: *European journal of cancer* 45.2, pp. 228–247.

Geus-Oei, Lioe-Fee de et al. (2006). "Comparison of Image-Derived and Arterial Input Functions for Estimating the Rate of Glucose Metabolism in Therapy-Monitoring 18F-FDG PET Studies". In: *Journal of Nuclear Medicine* 47.6, pp. 945–949. ISSN: 0161-5505. URL: http://jnm.snmjournals.org/content/47/6/945.full.

Grkovski, Milan et al. (2017). "Multiparametric Imaging of Tumor Hypoxia and Perfusion with 18F-Fluoromisonidazole Dynamic PET in Head and Neck Cancer." In: *Journal of nuclear medicine : official publication, Society of Nuclear Medicine* 58.7, pp. 1072–1080. ISSN: 1535-5667. DOI: 10.2967/jnumed.116.188649. URL: http://www.ncbi.nlm.nih.gov/pubmed/28183993http://www.pubmedcentral.nih.gov/articlerender.fcgi?artid=PMC5493008.

Gunn, Roger N., Steve R. Gunn, and Vincent J. Cunningham (2001). "Positron Emission Tomography Compartmental Models". In: *Journal of Cerebral Blood Flow & Metabolism* 21.6, pp. 635–652. ISSN: 0271-678X. DOI: 10.1097/00004647-200106000-00002. URL: http://journals.sagepub.com/doi/10.1097/00004647-200106000-00002.

Herzog, Hans and Christoph Lerche (2016). "Advances in clinical PET/MRI instrumentation". In: *PET clinics* 11.2, pp. 95–103.

Knoll, Glenn F. (2010). *Radiation detection and measurement*. 4th ed. Hoboken N.J.: John Wiley, p. 830. ISBN: 9780470131480. URL: https://www.worldcat.org/title/radiation-detection-and-measurement/oclc/612350364.

Knowland, Josh et al. (2018). "Practical Clinical Measurement of Radiotracer Concentration in Blood - Initial Device Concept and Feasibility Testing." In: *Journal of nuclear*

medicine technology, jnmt.118.212266. ISSN: 1535-5675. DOI: 10.2967/jnmt.118.212266. URL: http://www.ncbi.nlm.nih.gov/pubmed/30139882.

Kotasidis, Fotis A., Charalampos Tsoumpas, and Arman Rahmim (2014). "Advanced kinetic modelling strategies: towards adoption in clinical PET imaging". In: *Clinical and Translational Imaging* 2.3, pp. 219–237. ISSN: 2281-5872. DOI: 10.1007/s40336-014-0069-8. URL: http://link.springer.com/10.1007/s40336-014-0069-8.

Kriplani, A. et al. (2005). "Noninvasive high-resolution detection of the arterial and venous input function through a PET Wrist Scanner". In: *IEEE Nuclear Science Symposium Conference Record* 4.January, pp. 2240–2244. ISSN: 10957863. DOI: 10.1109/NSSMIC.2005.1596780.

Kriplani, A. et al. (2006). "Non-invasive and selective measurement of the arterial input function using a PET Wrist Scanner". In: *2006 IEEE Nuclear Science Symposium Conference Record*, pp. 3266–3270. DOI: 10.1109/NSSMIC.2006.353705. URL: http://ieeexplore.ieee.org/lpdocs/epic03/wrapper.htm?arnumber=4179747.

Lee, Nancy et al. (2016). "Strategy of Using Intratreatment Hypoxia Imaging to Selectively and Safely Guide Radiation Dose De-escalation Concurrent With Chemotherapy for Locoregionally Advanced Human Papillomavirus–Related Oropharyngeal Carcinoma". In: *International Journal of Radiation Oncology*Biology*Physics* 96.1, pp. 9–17. ISSN: 0360-3016. DOI: 10.1016/J.IJROBP.2016.04.027. URL: https://www.sciencedirect.com/science/article/pii/S0360301616301778.

Leutz, Heinrich (1995). "Scintillating fibres". In: *Nuclear Instruments and Methods in Physics Research Section A: Accelerators, Spectrometers, Detectors and Associated Equipment* 364.3, pp. 422–448. ISSN: 0168-9002. DOI: 10.1016/0168-9002(95)00383-5. URL: https://www.sciencedirect.com/science/article/pii/0168900295003835ht
//reader.elsevier.com/reader/sd/pii/0168900295003835?token=
07F4ED2BA9589745F7082EBF0D1EB1A13E6763FD1AE0F6F8AB7BCDC8A196DD8BF6C3B3AE

Litton, J. E. and L. Eriksson (1990). "Transcutaneous measurement of the arterial input function in positron emission tomography". In: *IEEE Transactions on Nuclear Science* 37, pp. 627–628. DOI: 10.1109/23.106688.

Lüdemann, L et al. (2006). "Corrections of arterial input function for dynamic H ₂ ¹⁵ O PET to assess perfusion of pelvic tumours: arterial blood sampling versus image extraction". In: *Physics in Medicine and Biology* 51.11, pp. 2883–2900. ISSN: 0031-9155. DOI: 10.1088/0031-9155/51/11/014. URL: http://stacks.iop.org/0031-9155/51/i=11/a=014?key=crossref.69639ededce64bc7404a95fbcd372086.

Michaelis, Laura C and Mark J Ratain (2006). "Measuring response in a post-RECIST world: from black and white to shades of grey". In: *Nature Reviews Cancer* 6.5, p. 409.

Moon, Sun Young et al. (2016). "Feasibility Study of Source Position Verification in HDR Brachytherapy Using Scintillating Fiber". In: *Progress in Medical Physics* 27.4, p. 213. ISSN: 1226-5829. DOI: 10.14316/pmp.2016.27.4.213. URL: https://synapse.koreamed.org/DOIx.php?id=10.14316/pmp.2016.27.4.213.

Nakamura, K (2010). "Review of Particle Physics". In: *Journal of Physics G: Nuclear and Particle Physics* 37.7A, p. 075021. ISSN: 0954-3899. DOI: 10.1088/0954-3899/37/7A/075021. URL: http://stacks.iop.org/0954-3899/37/i=7A/a=075021?key=crossref.de0390bfb70101fa23c6dbe588ea1324.

Phelps, Michael E., John C. Mazziotta, and Heinrich R. Schelbert (1986). *Positron emission tomography and autoradiography : principles and applications for the brain and heart*. Raven Press, p. 690. ISBN: 0881671185. URL: https://inis.iaea.org/search/search.aspx?orig{_}q=RN:17082803.

Podgoršak, Ervin B et al. (2006). *Radiation physics for medical physicists*. Springer.

Strauss, Ludwig G. et al. (2007). "Assessment of quantitative FDG PET data in primary colorectal tumours: which parameters are important with respect to tumour detection?" In: *European Journal of Nuclear Medicine and Molecular Imaging* 34.6, pp. 868–877. ISSN: 1619-7070. DOI: 10.1007/s00259-006-0319-8. URL: http://link.springer.com/10.1007/s00259-006-0319-8.

Strauss, Ludwig G et al. (2011). "Impact of cell-proliferation-associated gene expression on 2-deoxy-2-[18 F] fluoro-D-glucose (FDG) kinetics as measured by dynamic positron emission tomography (dPET) in Colorectal Tumors". In: *Molecular Imaging and Biology* 13.6, pp. 1290–1300.

Strauss, MD, Leyun Pan, and Ludwig G StraussMD (2010). "Parametric imaging: a promising approach for the evaluation of dynamic PET-18 F-FDG studies-the DKFZ experience". In: *Hellenic journal of nuclear medicine* 13.1, pp. 18–22.

Swank, Robert K. and Warren L. Buck (1953). "The Scintillation Process in Plastic Solid Solutions". In: *Physical Review* 91.4, pp. 927–933. ISSN: 0031-899X. DOI: 10.1103/PhysRev.91.927. URL: https://link.aps.org/doi/10.1103/PhysRev.91.927.

Takesh, Mustafa (2012). "The Potential Benefit by Application of Kinetic Analysis of PET in the Clinical Oncology." In: *ISRN oncology* 2012, p. 349351. ISSN: 2090-567X. DOI: 10.5402/2012/349351. URL: http://www.ncbi.nlm.nih.gov/pubmed/23326682http://www.pubmedcentral.nih.gov/articlerender.fcgi?artid=PMC3541563.

Thorwarth, Daniela et al. (2005). "Kinetic analysis of dynamic 18F-fluoromisonidazole PET correlates with radiation treatment outcome in head-and-neck cancer". In: *BMC Cancer* 5.1, p. 152. ISSN: 1471-2407. DOI: 10.1186/1471-2407-5-152. URL: http://bmccancer.biomedcentral.com/articles/10.1186/1471-2407-5-152.

Tucker, Elizabeth W et al. (2018). "Noninvasive 11C-rifampin positron emission tomography reveals drug biodistribution in tuberculous meningitis." In: *Science translational medicine* 10.470, eaau0965. ISSN: 1946-6242. DOI: 10.1126/scitranslmed.aau0965. URL: http://www.ncbi.nlm.nih.gov/pubmed/30518610.

Turgeon, V., G. Kertzscher, and S. Abbasi Nejad Enger (2018). "Non-Invasive Positron Detector to Monitor the Input Function in PET". English. In: *MEDICAL PHYSICS* 45.6. 60th Annual Meeting of the American-Association-of-Physicists-in-Medicine, Nashville, TN, JUL 29-AUG 02, 2018, E174. ISSN: 0094-2405.

Turgeon, V, G Kertzscher, and Shirin A Enger (2018). "Non-Invasive Positron Detector to Monitor the Input Function in PET". In: *MEDICAL PHYSICS* 45.6, E174–E175.

Villanueva, A. et al. (2003). "Spatial resolution of a noninvasive measurement of the arterial and venous input function using a wrist monitor". In: *2003 IEEE Nuclear Science Symposium. Conference Record (IEEE Cat. No.03CH37515)*. IEEE, pp. 2232–2236. ISBN: 0-7803-8257-9. DOI: 10.1109/NSSMIC.2003.1352343. URL: http://ieeexplore.ieee.org/document/1352343/.

Wagenknecht, Gudrun et al. (2013). "MRI for attenuation correction in PET: methods and challenges". In: *Magnetic Resonance Materials in Physics, Biology and Medicine* 26.1, pp. 99–113. DOI: 10.1007/s10334-012-0353-4. URL: https://doi.org/10.1007/s10334-012-0353-4.

Watabe, H. et al. (1995). "Development of skin surface radiation detector system to monitor radioactivity in arterial blood along with positron emission tomography". In: *IEEE Transactions on Nuclear Science* 42.4, pp. 1455–1459. ISSN: 00189499. DOI: 10.1109/23.467729. URL: http://ieeexplore.ieee.org/lpdocs/epic03/wrapper.htm?arnumber=467729.

Watabe, H et al. (2001). "Noninvasive estimation of the aorta input function for measurement of tumor blood flow with." In: *IEEE transactions on medical imaging* 20.3, pp. 164–74. ISSN: 0278-0062. DOI: 10.1109/42.918468. URL: http://www.ncbi.nlm.nih.gov/pubmed/11341707.

Watabe, Hiroshi et al. (2006). "PET kinetic analysis compartmental model". In: *RE-VIEW Annals of Nuclear Medicine* 20.9, pp. 583–588. URL: https://link.springer.com/content/pdf/10.1007{\%}2FBF02984655.pdf.

White, T.O. (1988). "Scintillating fibres". In: *Nuclear Instruments and Methods in Physics Research Section A: Accelerators, Spectrometers, Detectors and Associated Equipment* 273.2-3, pp. 820–825. ISSN: 01689002. DOI: 10.1016/0168-9002(88)90102-7. URL: https://linkinghub.elsevier.com/retrieve/pii/0168900288901027.

Williamson, Jeffrey F. (2018). "Fundamentals of Ionizing Radiation Dosimetry. PAndreo, DTBurns, AENahum, JSeuntjens, FHAttix. Weinheim, Germany: Wiley-VCH,

2017. 957. pp. Price: $215.00. ISBN: 978-3-527-40921-1." In: *Medical Physics* 45.11, pp. 5353–5354. ISSN: 0094-2405. DOI: 10.1002/mp.13164. URL: https://onlinelibrary.wiley.com/doi/abs/10.1002/mp.13164.